2020

REDUCED-ORDER CHARACTERIZATION OF THE AEROELASTIC RESPONSE OF STALL-CONTROLLED WIND TURBINES UNDER ATMOSPHERIC TURBULENCE

Sara Jalal
Michigan Technological University, sjalal@mtu.edu

REDUCED-ORDER CHARACTERIZATION OF THE AEROELASTIC RESPONSE OF STALL-CONTROLLED WIND TURBINES UNDER ATMOSPHERIC TURBULENCE

By

Sara Jalal

A DISSERTATION

Submitted in partial fulfillment of the requirements for the degree of

DOCTOR OF PHILOSOPHY

In Mechanical Engineering - Engineering Mechanics

MICHIGAN TECHNOLOGICAL UNIVERSITY

2020

This dissertation has been approved in partial fulfillment of the requirements for the Degree of DOCTOR OF PHILOSOPHY in Mechanical Engineering - Engineering Mechanics.

Department of Mechanical Engineering - Engineering Mechanics

Dissertation Advisor:	*Dr. Fernando L. Ponta*
Committee Member:	*Dr. Leonard J. Bohmann*
Committee Member:	*Dr. Hassan Masoud*
Committee Member:	*Dr. Sajjad Bigham*
Department Chair:	*Dr. William W. Predebon*

Dedication

To my Parents for their unconditional love and support.

Without their support, I may not have found myself at this stage of life

Contents

List of Figures

Acknowledgments

It is indeed a great privilege to have worked under the guidance of Dr. Fernando L. Ponta for my doctoral research. He has been an excellent mentor, a good friend, and a remarkable source of inspiration to pursue scientific research. I am grateful for his passion and continuous support throughout the course of my degree. I would like to sincerely thank my doctoral advisory committee, Dr. Hassan Masoud, Dr. Leonard J. Bohmann, and Dr. Sajjad Bigham for their interest in this research.

I would like to thank the Department of Mechanical Engineering - Engineering Mechanics for providing me with opportunities to teach and guide undergraduate students, which also supported my educational expenses. The dedication of the departmental staff in many occasions made things easier, and I'm grateful for their support. The Doctoral Finishing Fellowship awarded through the Graduate School at Michigan Technological University was a great opportunity to focus on timely completion of the degree.

I am extremely thankful to the WindGroup research team in the department of Mechanical Engineering - Engineering Mechanics for the constant support and criticisms. The numerous brainstorming sessions and philosophical discussions have shaped me into a better researcher.

Definitions

h	Hub coordinate system
L	Blade reference line (longitudinal axis) in non-deformed configuration
l	Blade reference-line in deformed configuration
α	Angle of attack of wind
W	Velocity of wind
ρ	Density
C_l	Coefficient of Lift
C_d	Coefficient of Drag
C_m	Coefficient of Pitching Moment
C_t	Aerodynamic coefficient of force in chord-wise direction
C_n	Aerodynamic coefficient of force in chord-normal direction

List of Abbreviations

BEM	Blade Element Momentum
CFD	Computational Fluid Dynamics
CODEF	Common Ordinary Differential Equation Framework
DRD-BEM	Dynamic Rotation Deformation - Blade Element Momentum
DU	Delft University
FCD	Flow-control device
GTBM	Generalized Timoshenko Beam Model
HAWT	Horizontal Axis Wind Turbine
IEC	International Electrotechnical Commission
kN	kilo-Newton
kW	kilo-Watt
MW	Mega-Watt
NACA	National Advisory Committee for Aeronautics
NREL	National Renewable Energy Laboratory
ODE	Ordinary Differential Equation
RPM	Revolutions per minute
RWT	Reference Wind Turbine
TS	Technical Specification

Abstract

Wind, by its vary nature, varies with place and time, making energy conversion difficult. This calls for the development of improved technologies that efficiently harness energy from the available wind resource, and advanced control systems are a key research aspect of wind turbine technology. Such systems are needed to maximize the rotor's output power at wind speeds below the nominal value for the turbine, limit rotor power at wind speeds higher than the nominal, and reduce fluctuating loads on the turbine blades that may compromise their long-term operational life. Among the several families of control methods for wind turbines, Pitch and Stall are by far the most used in modern utility-scale machines. Both are based on altering the aerodynamic characteristics of the blade sections in order to control the forces which produce the rotor's torque, power, and thrust, and its deformation. A very popular control method to optimize power production and control is using Variable- Speed Wind Turbines (VSWT) a relatively new idea, which offers has a promising perspective for future applications. As with the classical Fixed-Speed (FS) stall method lowers the capital cost and reduces maintenance expenses, while at the same time, allows for a more efficient and precise control of power production. This research investigated the aeroselastic behavior of the stall-controlled rotors, studied the frequency content and time evolution of their oscillatory behavior, and gained a better understanding of

the underlying physics. This calls for a wide range of experiments that assess the effects of rapid variations on the rotor's operational conditions, like gusts and turbulent fluctuations on the wind flow. To systematize this analysis, various gust conditions tested for different wind speeds. These are represented by pulses of different intensity, occurring suddenly in and otherwise constant wind regime. This allows us to observe the pure aero-elasto-inertial dynamics of the rotor's response. We will show the results from an extensive series of experiments analyzing the aeroelastic response of the rotor to wind speed fluctuations associated to the turbulent characteristics of the atmospheric boundary layer, focusing on obtaining a reduced-order characterization of the rotor's dynamics as an oscillatory system based on energy-transfer principles. Besides on its intrinsic scientific value, this aspect of the work presented here is of fundamental interest for researchers and engineers working on developing optimized control strategies for wind turbines. It allows for the critical elements of the rotor's dynamic behavior to be described as a reduced-order model that can be solved in real-time, an essential requirement for determining predictive control actions.

Chapter 1

Introduction

Renewable energy production, especially wind power, has been growing over time to become an important source to provide for electricity and fuel demands [4]. Technological advances have made wind the fastest growing renewable energy technology in electricity generation systems [5]. One of the remarkable advantages of wind energy, in comparison with other renewable sources, is the lack of harmful emissions and reduced harm to the environment along its entire life-cycle. Its continuously decreasing costs have made wind energy competitive with other energy resources, including several conventional sources like nuclear or coal [6, 7].

Following the current global trend of the wind turbines to be commissioned and the studies conducted by the European Wind Energy Association (EWEA), the next

generation of state-of-the-art turbines would have a generating capacity of 20 MW with rotor diameters upwards of 250 m [8]. According to [9] between the years of 2000 to 2007 the installed capacity increased from 14,604 MW to 84,934 MW. Moreover the systematic increase in rotor size is prompted by economies-of-scale factors thereby resulting in the continuously decreasing cost per kWh generated. However, such large rotors have larger masses associated with them and necessitate studies to better understand their dynamics. This has led to numerous efforts on developing suitable control approaches [10, 11, 12]. Bianchi et al. [13] have provided details on some common load control methodologies. Those being currently studied and implemented are stall control [14], pitch control [15, 16, 17], active stall control [18], passive control using aeroelastic devices [19], and active yaw control [20, 21].

Wind, by its vary nature, varies with place and time, making energy conversion difficult. This calls for the development of improved technologies that efficiently harness energy from the available wind resource, and advanced control systems are a key research aspect of wind turbine technology [22]. Such systems are needed to maximize the output power at low wind speeds, limit rotor power at wind speeds above the nominal value, and reduce fluctuating loads on the turbine blades that may compromise their long-term operational life [23]. Among the several families of control methods for wind turbines, Pitch and Stall are by far the most used in modern utility-scale machines. Both are based on altering the aerodynamic characteristics of the blade sections in order to control the forces which produce the rotor's torque,

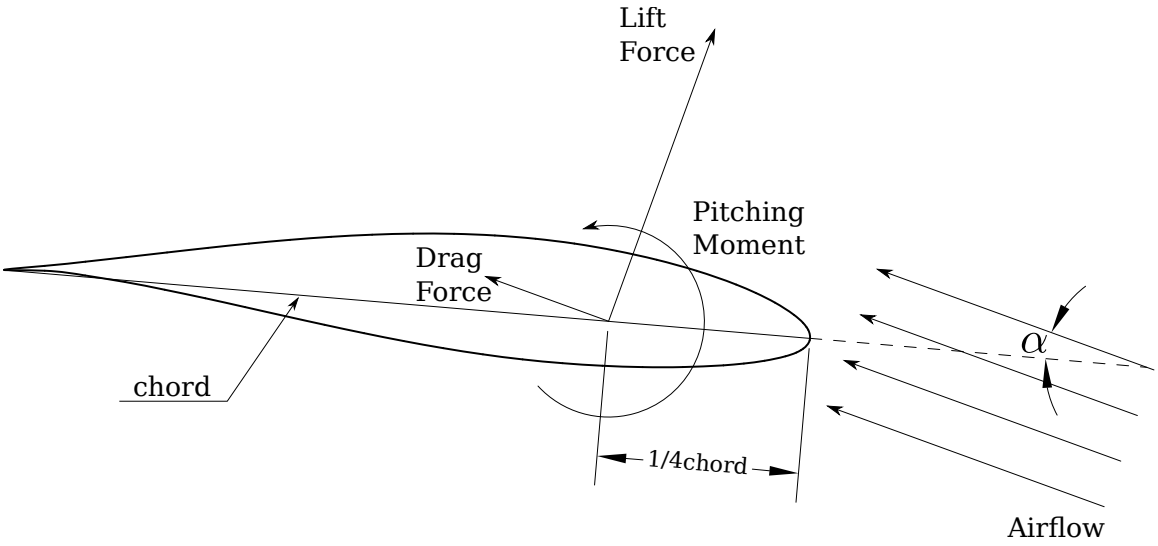

Figure 1.1: Basic aerodynamic parameters on an airfoil section.

power, and thrust, and its deformation.

Let's start with reviewing the aerodynamics of an airfoil shape on a blade section, its various geometrical parameters, the flow velocities, and the associated aerodynamic forces acting on the blade. More details about rotor aerodynamic theory can be found in Manwell et al. [24] and Burton et al. [25]. Figure 1.1 shows a generic airfoil shape and the main aerodynamic forces resulting from an incoming airflow. The chord is defined as the line connecting the leading edge and the tip of the airfoil. The angle between the incoming airflow and the chord is called angle of attack and is denoted by α. The resultant of all of the pressure and friction forces acting along the airfoil surface are two forces, and a moment with respect to a point on the chord-line at a distance of $c/4$ ("quarter-chord") from the leading edge.

The Lift force is a consequence of the unequal pressure on the upper and lower airfoil surfaces and its direction is perpendicular to the oncoming airflow direction. The Drag force is due to both, pressure and viscous-friction forces at the surface of the airfoil and its direction is parallel to the direction of oncoming airflow. In terms of energy production and power control, the two important aerodynamic forces are lift and drag, given by $dF_{lift} = \frac{1}{2}\,\rho\,C_l\,W_{rel}^2\,c$ and $dF_{drag} = \frac{1}{2}\,\rho\,C_d\,W_{rel}^2\,c$, where the lift coefficient, C_l, and drag coefficient, C_d, depend on the airfoil profile and the angle of attack, α, c is the chord length, ρ is the air density, and W_{rel} is the velocity of the incoming flow.

In a basic analysis of the flow around a blade section, there are two main velocity components that define the incoming airflow: one is the local velocity of the wind at the point of crossing the rotor's plane, and the other is the tangential component due to the rotation of the blade itself. Figure 1.2 shows a wind turbine airfoil cross-section under working conditions with all associated velocities, forces and angles. The entities in this figure are: Ω, which indicates the magnitude of the angular velocity and whose axis of rotation coincides with the rotor's rotational axis; the incoming wind which is essentially parallel to the rotor's axis and has a magnitude of $W_\infty\,(1-a)$, where W_∞ is the velocity of the undisturbed wind upstream of the rotor and a is the axial induction factor, which indicates the velocity loss due to the presence of the rotor; and the tangential velocity given by $\Omega\,r$, where r is the distance from the airfoil section to the rotor axis. Using this scheme we are going to explain the basic

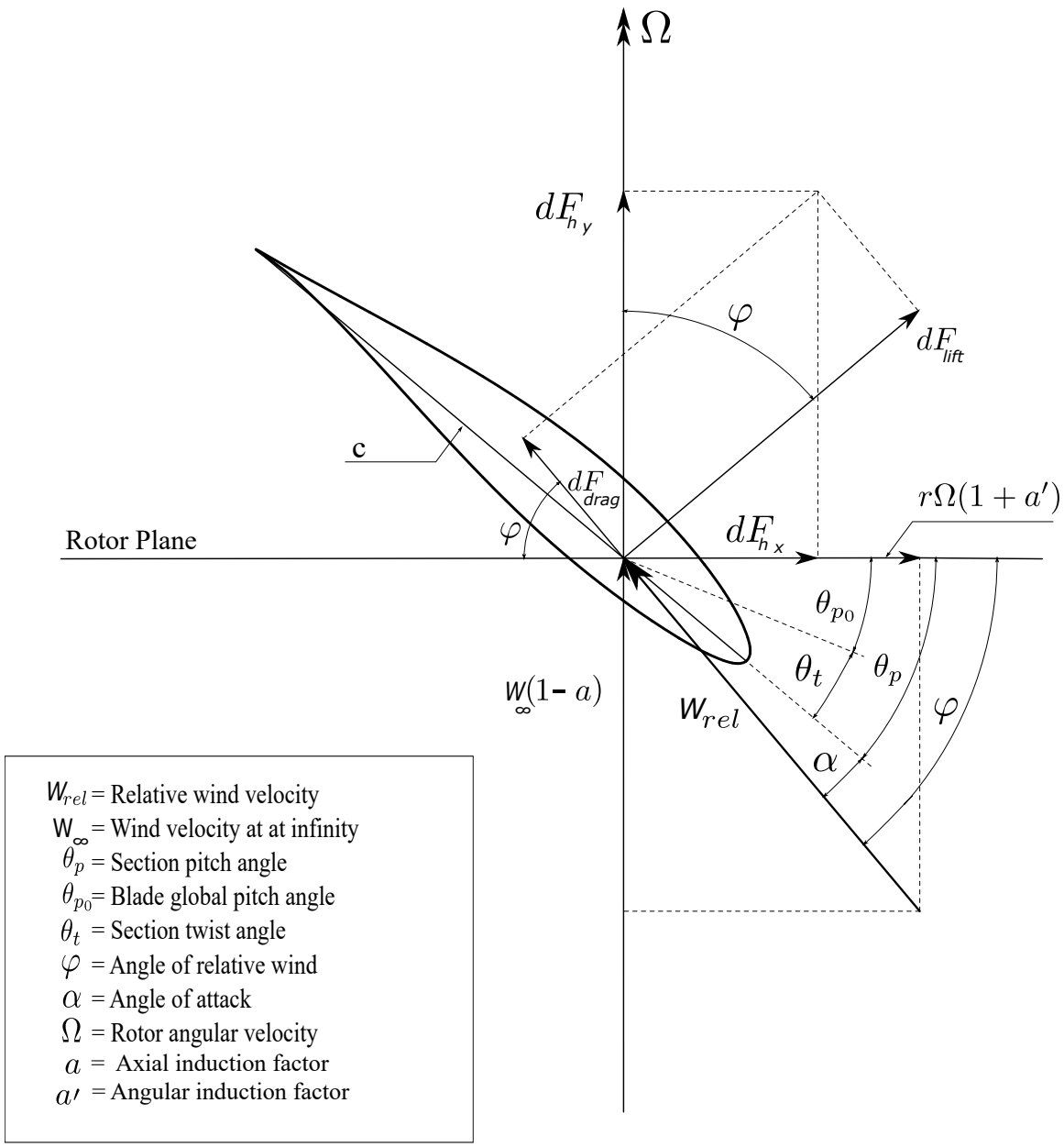

Figure 1.2: Schematic of velocities and forces on the cross-section of a wind turbine blade.

physical mechanism underlying the operation of the two most popular families of control methods: Pitch and Stall [6]. In all cases, the basic objective is to maximize the rotor's power production for wind speeds below the nominal, and limit it for wind

Figure 1.3: Pitch control action

speeds above the nominal; keeping it as close as possible to the nominal power of the drive train, in order to avoid exceeding the nominal power of shafts, bearings, gear box, generators, and power electronics.

By rotating the blades around their root (see figure 1.3), pitch-control systems allow us to smoothly change the aerodynamic forces acting on the blade by altering the angle of attack on the airfoil blade sections. Hence, changing the tangential projection of the aerodynamic force (which is the one contributing to the driving torque), we can smoothly control the rotor's output power. In terms of the schematic in figure 1.2, by changing the pitch angle of the whole blade, θ_{p0}, we modify the pitch angle for each

one of the blade sections θ_p. This, in turns, modifies the angle of attack α, which is given by the difference between θ_p and the angle of incoming flow φ. For instance, a pitching action increasing θ_{p_0} will reduce α, and hence the lift force on the blade section dF_{lift}. This also reduces the tangential projection, dF_{h_x}(i.e., projection of the aerodynamic force onto the plane of rotation). By reducing dF_{h_x}, there is a reduction in the driving torque contributed by each one of the blade sections, producing a total reduction in the driving torque of the whole turbine. Figure 1.4 shows an example of a typical the power curve for a pitch-controlled machine (P/P_{nom} indicates rotor's generated power normalized by its nominal value).

In stall control turbines, the blades are rigidly attached to the hub. Thus, θ_p, and hence θ_{p_0}, are fixed for every section along the blade span. In the classic *fixed-speed* stall control method, the rotational speed of the rotor is kept constant at its nominal value, and the geometry of the blades is designed in such a way that, as the wind speed increases above the nominal value, an increasing portion of the blade span enters into stall. The stall condition is characterized by the separation of the boundary layer on the rear-upper surface of an airfoil section at high angles of attack. Separation disrupts the flow circulation and alters the pressure distribution, drastically reducing lift and increasing drag. The overall result is that those portions of the blade span that enter into stall stop contributing to the driving torque, limiting the rotor's power production.

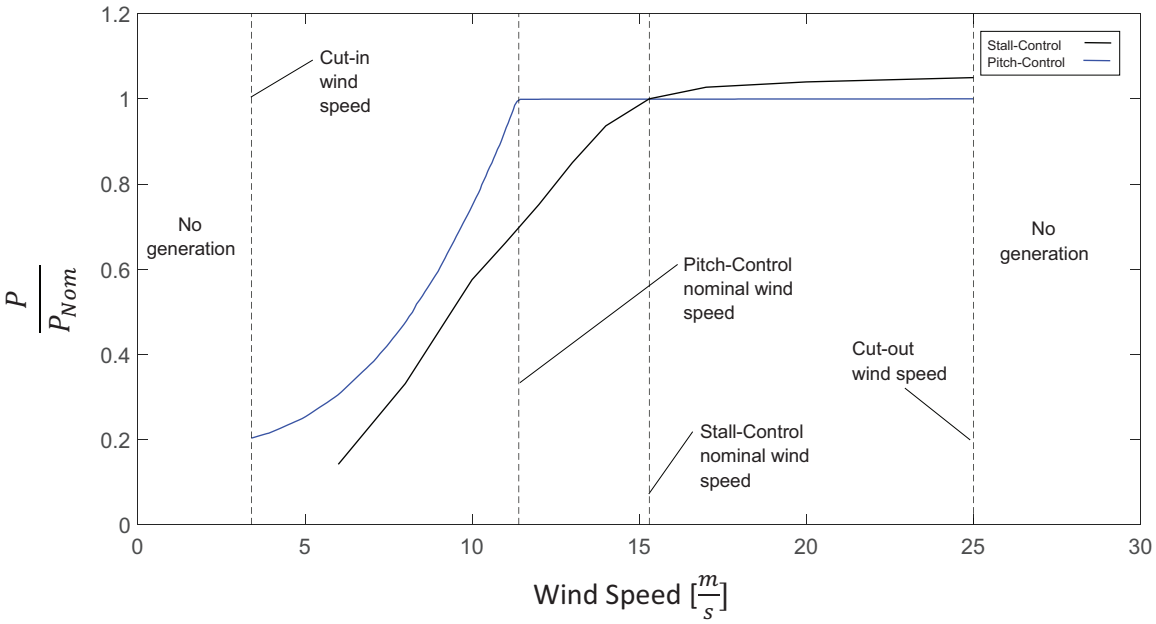

Figure 1.4: Examples of typical power curves and wind-speed ranges of operation for Pitch- and Stall-controlled turbines

In terms of figure 1.2, if we keep Ω constant, the tangential component of the relative wind $r\,\Omega\,(1+a')$, for a given radial position along the span remains practically constant too (except for small variations of the angular induction factor a'). As the wind speed W_∞ increases, so does the axial component of the relative wind (i.e., the component normal to rotor plane $W_\infty\,(1-a)$). Even accounting for some variation of the axial induction factor a, this results in an increase of the angle of incidence of the relative wind φ. Since the pitch angle for every section, θ_p is fixed, this ultimately leads to an increase in the angle of attack α beyond the stall limit, and to the separation of the boundary layer.

In terms of the forces diagram of figure 1.2, separation leads to a substantial reduction

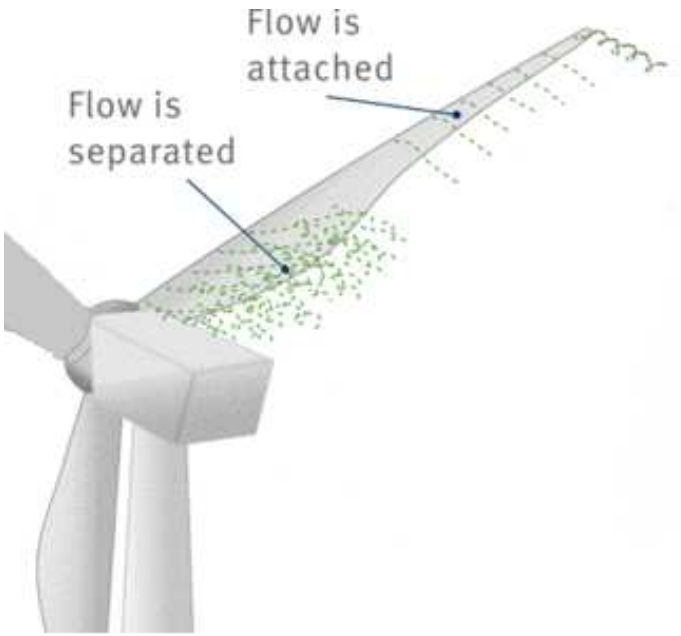

Figure 1.5: Flow regimes over a Stall-control blade

in the lift dF_{lift} and an increase in the drag dF_{drag}. This decreases the tangential (i.e., the in-plane) projection of the total aerodynamic force on that blade section, F_{h_x}, which is the one contributing to the driving torque. Moreover, if the lift continues decreasing and the drag increasing, F_{h_x} can decrease to a point that it becomes negative. That means that particular blade section not only stops contributing to the driving torque, but could also act as a brake. In this process, the axial projection of the aerodynamic force, dF_{h_y}, can also vary, but since it is co-linear with the main shaft, it only affects the thrust on the rotor, and it is inconsequential for the analysis of power production.

It is important to note that the stall transition is not intended to occur simultaneously all over the span. Separation of the boundary layer is an abrupt phenomenon, accompanied by sudden changes in the aerodynamic forces. That is, the geometry is not designed in such a way that the whole blade instantaneously flips between the stall and the attached regime, because that would induce dynamic shocks making the rotor uncontrollable. The stall-control method works by gradually changing the portions of the blade span that are either in stall or attached regimes.

Figure 1.5 shows a schematic representation of the airflow regime over the blade along different sections of the span, with the inner section of the blade in stall, and the outer sections in attached regime. Due to shorter radius of the inner sections of the blade, their tangential speed is lower. This implies that the inner sections of the blade, especially those very close to the root, have a higher tendency to enter into stall. Also, as the inner sections of the blade are very thick (sometimes very similar to cylindrical shapes), their boundary layers are usually separated because they behave as bluff bodies. On the other hand, in the outer part of the blade, from the transitional zone to the tip, the flow is attached. This portion of the span where the flow is attached could be called the *aerodynamically-active* part of the blade. These are the span regions which mostly contribute to the total driving torque of the turbine.

The stall control method works by allowing the transition between the separated flow

region and the attached flow region to gradually move along the span, changing the portion of the blade that positively contributes to the driving torque. For instance, in power-limiting mode, as the wind speed increases, the transitional boundary between the two zones gradually moves outwards toward the tip of the blade. Thus allowing for a smooth limitation of power production. Figure 1.4 shows an example of a typical power curve for a fixed-speed stall-controlled machine. Note that the classic fixed-speed stall method is not as smooth or precise as the pitch method in terms of power control, and its energy-conversion efficiency at wind speeds lower than the nominal is lower.

1.1 Variable Speed Wind Turbines

A very popular control method to optimize power production and control is using Variable-Speed Wind Turbines (VSWT) that allow changing the rotational speed (rpm) of the rotors as part of their control strategy. Having a wind turbine that can work at different rotational speeds, has several advantages. In terms of optimizing power harvesting, it allows a finer *tuning* of the aerodynamic conditions on the blade sections at different wind speeds, by adjusting the tangential component of the relative wind (see figure 1.2). In terms of implementing practical pitch control systems, it allows the turbine to increase revolutions in the event of a gust, using the rotor as a flywheel to absorb the sudden increase of kinetic energy. This acts as a buffer to

provide time for the pitch mechanism to act and limit the rotor's driving torque, giving a smooth control of power production. If that buffer action didn't exist, there would be no practical way for a pitching device to act in real time to exert the control action on the big massive blades of today's utility-scale turbines. For these reasons, variable-speed pitch control has substantially grown in popularity during the last two decades, to become the preferred method to control wind turbines with power levels of 1.5 MW and above [26].

VSWTs use power electronics and aerodynamic devices to simultaneously control torque, power and rotational speed of the rotor and the generator. The quality of electrical power produced is improved, and torque fluctuations are limited, which reduces the stresses caused by wind gusts [15]. Involving a more complex combination of factors, the control strategy has a significant role in this kind of wind turbine. VSWTS can function at near maximum efficiency in low-to-moderate wind speeds due to the highly optimized blade rotation speed thereby ensuring maximum power generation. [27]. They also can increase energy capture by about 5-10% [28].

The proportion of wind kinetic power that can be harvested by a turbine is quantified by a non-dimensional quantity called the Power Coefficient, C_p. The power produced by the rotor could be written as $P = 1/2 C_p A \rho W_\infty^3$, where ρ is the air density, and A is the swept area of the rotor [14]. Among other aspects related with the aerodynamics of the blades (like their aspect ratio, or the efficiency of their airfoil sections), C_p is

affected by the relation between the wind speed and the angular speed of the rotor. This is quantified by a non-dimensional factor called the *tip speed ratio*, computed as $\lambda = \frac{R\Omega}{W_\infty}$, where R is the radius of the rotor. It computes the ratio between the tangential speed of the blade's tip and the undisturbed wind speed. In any rotor design, for each specific wind speed, there is a specific rotational speed which ensures the maximum output power [29]. In VSWTs, the capability of adjusting the turbine's rotational speed, gives an advantage in terms of optimizing their Cp under different wind conditions.

1.2 Pitch Control Method vs Stall Control Method

In the present study, we focus on the Variable-Speed (VS) stall control method, a relatively new idea, which offers a promising perspective for future applications. As with the classical Fixed-Speed (FS) stall method, the elimination of the pitch mechanism, lowers the capital cost and reduces maintenance expenses, while at the same time, allows for a more efficient and precise control of power production [26].

The elimination of the pitching mechanism is particularly important when considering the systematic increase in turbine size that has been taking place during the last 30 years. This process, sometimes referred to as *upscaling*, is prompted by economies of

scale which reduce the cost of wind energy, and is likely to continue in the future. One of the consequences of upscaling is the substantial increase of blade mass per unit energy produced, as blade mass depends on the cube of the rotor's diameter, while energy capture depends on rotor's swept area (i.e., the diameter's square). In addition to construction and materials cost aspects, this so-called *square-cube law* implies that the size and cost of the pitching mechanisms (and the energy required for their actuation) would increase much faster than the increase in the energy produced, as turbine size increases. Thus, elimination of pitch mechanisms by adopting some form of stall control would represent a big advantage for the the next generation of high capacity wind turbines with much larger blades [30].

As it was mentioned above in reference to the power curves in figure 1.4, classic fixed-speed stall is not as precise as pitch in terms of power control and energy-conversion efficiency at low wind speeds. The main advantage of using VS stall versus the classical FS stall is that we obtain the capacity of exerting a finer control on the rotor's driving torque to limit power output for wind-speeds above the nominal, and to optimize energy capture for wind speeds below the nominal. In terms of the diagram in figure 1.2, if we had the capacity of varying the turbine's rotational speed Ω, we could control the tangential projection of the relative wind velocity, and hence, its angle of incidence φ, which in turn determines α. This allows us to precisely control the portion of the blade span that enters into stall. For instance, at low wind speeds, we may over-rev the turbine above its nominal rpm to reduce φ (and hence α),

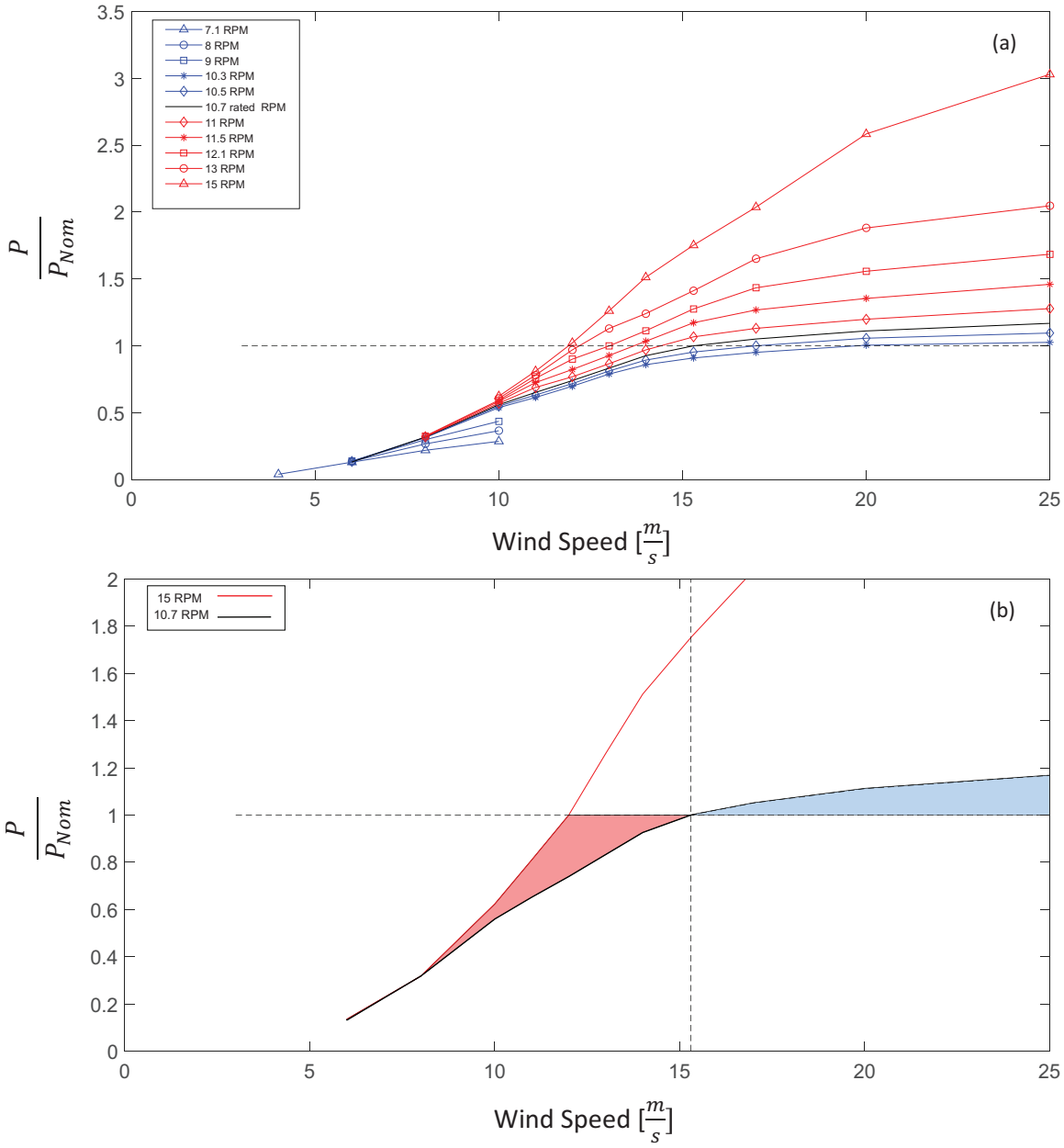

Figure 1.6: (a): Power output curves at different rotational speeds for stall-control rotor of the DU-5MW RWT, (b): advantages of VS stall versus FS stall.

in such a way to re-attach the flow over sections of the blade that otherwise would be in stall. This would increase the driving torque and thus power output. Conversely, at high wind speeds, we may under-rev the turbine below its nominal rpm to generate the opposite effect, increasing α, and inducing a larger portion of the span to stall, in such a way as to keep the power output flat at nominal level.

Figure 1.6(a) shows a series of plots of power output computed at different rotational speeds, for the alternative stall-control rotor proposed by the Delft University (DU) [31] as a substitute for the original pitch-control rotor of the benchmark NREL-5MW Reference Wind Turbine (RWT) [32]. The DU-5MW stall RWT has a nominal wind speed of 15.3 m/s, and a nominal rotational speed of 10.7 rpm when operating in its original FS stall mode. The black curve represents the power output of the original fixed-speed design operating at 10.7 rpm, red curves represent power output at higher rotational speeds, and blue curves at lower rpm.

When the turbine is working in FS stall mode, power production at a the nominal 15.3 m/s wind is optimal, but the rotor starts loosing power-conversion capacity when the wind speed falls below the nominal. This is because, in the absence of any variable-geometry device like the pitch change, the rotor looses aerodynamic efficiency as it moves off its optimal design point. If we operated this same rotor in VS stall, we could have changed the rpm, switching into the red curves, to maximize the energy production at low wind speeds up to the nominal value which the drive train can

safely handle. At high wind speeds, we can switch to the blue curves at lower rpm, to keep power output flat at its nominal value.

Figure 1.6(b) summarizes the advantages of VS stall versus its classical FS predecessor: The area shaded in red represents what we gain by using variable speed in terms of improved energy-capture. This improvement is not trivial, especially when we consider the substantial number of hours per year that the wind speed falls below the nominal range in a typical wind-speed statistical distribution. Above the nominal wind speed, the blue region represents what we get in terms of a better and more stable limitation of power output. In this case, the change in rpm is relatively low, but the consequential power reduction is substantial, which makes VS stall a powerful tool to keep the power output at safe levels. We are going to revisit this topic in connection with the aeroelastic study in chapter 5.

1.2.1 Fixed Speed stall wind Turbine

The notion of fixed speed in stall control comes mostly because the speed is very close to be fixed on the aerodynamic side essentially the wins turbine rotor but from the electrical point of view that task is performed by an induction or synchronous generator. The classical squired cage has no way of controlling the slip and it has a very stiff torque to the rpm, that means in all the range of operation of the machine

from zero power to nominal power the angular speed of the rotor changes very little with respect to the reference synchronous speed or angular speed of the magnetic field created in the stator.

When it is acting as a motor, the torque is positive and the part of the curve from zero rpm until synchronous rpm which in the case of 60Hz and 4 poles, it is going to be 1800rpm when you go beyond that the machine stops to produce mechanical torque and absorb electrical energy and starts to produce mechanical electric energy by absorbing mechanical torque, essentially to over rev it to beyond the synchronous speed and the machine starts to what they called take load. In that case, it means the wind turbine rotor is turning such a way that after the gearbox multiples that speed the rotor of the electrical machine turns above 1800rpm and then the electrical machine starts to absorb mechanical power essentially act as a brake on the wind turbine rotor.

1.2.2 Variable Speed stall wind Turbine

Instead of squirrel cage rotor, you have winding rotor in this asynchronous,induction generator and those windings are connected to the grid not directly, the windings on the stator is still connected through on inventor is in that way you can either absorb or deliver electricity from the rotor on the grid (exchange energy in the grid). Usually

you produce electricity with that so approximately 30-35% of the delivered by the electrical machine to the grid is processes by this power electronic this inventor and comes from the rotor and the rest comes from the stator (only part of the machine connected to the grid).

The advantages of this is you can control the slip between the rotational speed with respect to the synchronous frequency of the stator, so the stator is still producing magnetic field that is rotating at 1800rpm but now the slip is not just 50rpm it could b more control and that allow to control mechanical rpm of the turbine by controlling the mechanical rpm of the electrical rotor on the generator. That allows us to control ω and then ϕ

1.3 Focus of study

With the ever growing demand for energy, even with wind being the fastest growing source of energy, its variations with time and place are of significant barriers to maximizing energy conversion. This calls for the development of improved technologies that efficiently harness energy from the available wind resource, and advanced control systems are a key research aspect of wind turbine technology.

This research is the investigation of the aeroselastic behavior of the stall-controlled

rotors, and the study of the frequency content and time evolution of their oscillatory behavior, and to gain a better understanding of the underlying physics. This called for a wide range of experiments to assess the effects of rapid variations on the rotor's operational conditions, like gusts and turbulent fluctuations on the wind flow. To systematize this analysis, various gust conditions were tested for different wind speeds. These are represented by pulses of different intensity, occurring suddenly in and otherwise constant wind regime. This allowed us to observe the pure aero-elasto-inertial dynamics of the rotor's response. We will show the results from an extensive series of experiments analyzing the aeroelastic response of the rotor to wind speed fluctuations associated to the turbulent characteristics of the atmospheric boundary layer, focusing on obtaining a reduced-order characterization of the rotor's dynamics as an oscillatory system based on energy-transfer principles. Besides on its intrinsic scientific value, this aspect of the work presented here is of fundamental interest for researchers and engineers working on developing optimized control strategies for wind turbines. It allows for the critical elements of the rotor's dynamic behavior to be described as a reduced-order model that can be solved in real-time, an essential requirement for determining predictive control actions. Our results and the different oscillatory behaviors under atmospheric turbulence and conclusions are presented in this dissertation.

1.4 Thesis outline

Chapter 1 provides a background on the significance of utility-scale wind turbines, some commonly used load control techniques. Chapter 2 presents the basic theoretical background of the Dynamic Rotor Deformation-Blade Element Momentum (DRD-BEM) model, which couples the aerodynamic and structural models as one dimensional model. Chapter 3 presents a preliminary study on the aeroselastic behavior of the stall-controlled VSWT rotors, study the frequency content and time evolution of their oscillatory behavior, and the span distribution of the flow regime in terms of its stall characteristics. In chapter 4 we will discuss the statement of the problem form the point of view of the typical variations in wind conditions a wind turbine operates, and starting with the main characteristics of gusts and atmospheric turbulent fluctuations in terms of amplitude and frequencies.

Chapter 5 will show the results from an extensive series of experiments analyzing the aeroelastic response of the rotor to wind speed fluctuations associated to the turbulent characteristics of the atmospheric boundary layer, focusing on obtaining a reduced-order characterization of the aero-elasto-inertial dynamics of the rotor as an oscillatory system based on energy-transfer principles. This last aspect of the work presented here is of fundamental interest for researchers and engineers working on developing optimized control strategies for wind turbines. It allows for the critical

elements of the rotor's dynamic behavior to be described as a reduced-order model that can be solved in real-time, an essential requirement for determining predictive control actions.

Finally, in chapter 6 we will cover the concluding remarks and discuss an outlook for further work. In order to keep the flow of the narrative in Chapter 5, we selected a subset of the experimental results to illustrate the nature of the reduced-order characterization and the energy-transfer principle. These results are complemented by an extended series of plots over the complete range of wind speeds shown in two appendices: Appendix A for the stable regime, and Appendix B for the unstable regime.

Chapter 2

Fundamentals of the Numerical Model Employed in this Work

This chapter presents the basic theoretical background of the Dynamic Rotor Deformation-Blade Element Momentum (DRD-BEM) model [33], which couples the aerodynamic and structural models as one dimensional model.

Several models have been proposed for simulating the flow across a wind turbine. These can be narrowed down to two major lines of approach. The first is based on a Stream-Tube model where the blade forces (represented by a virtual surface called an "actuator") are equated to the change in momentum on a Stream-Tube that encloses the turbine's swept area (see figure 2.1). The second approach consists

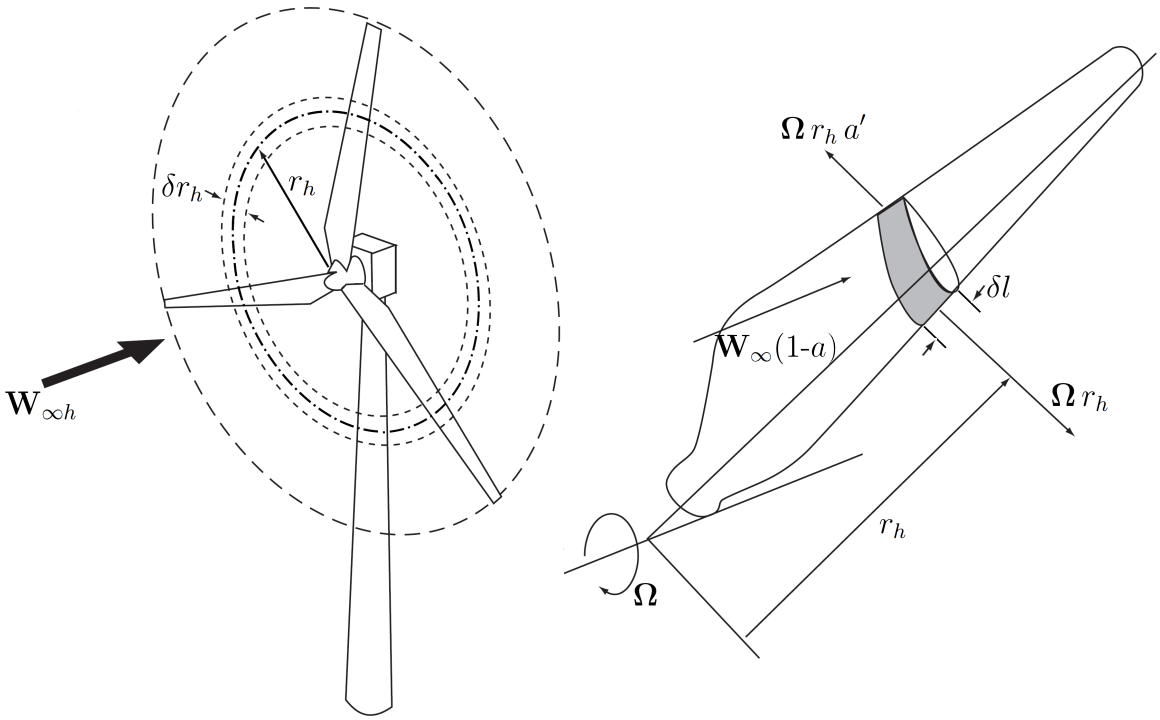

Figure 2.1: Schematic view of the dynamic generation of the annular actuator swept by a blade element

of representing the blades and their wakes by a set of vortex elements (see [34] for a detailed discussion). Among the stream-tube family, the Blade Element Momentum model (BEM) [24, 25] is the most common tool used in the design and analysis of horizontal axis wind turbines (HAWTs), proposed almost a century ago [35, 36]. Although some corrections and improvements have been applied to this model along the years [37, 38, 39], its main theoretical basis has remained the same

The classical BEM implementation works on the assumption that the blade sections are perpendicular to a radial line in the rotor's plane. Because of this assumption, the classical BEM cannot consider misalignments of the blade sections. This can lead

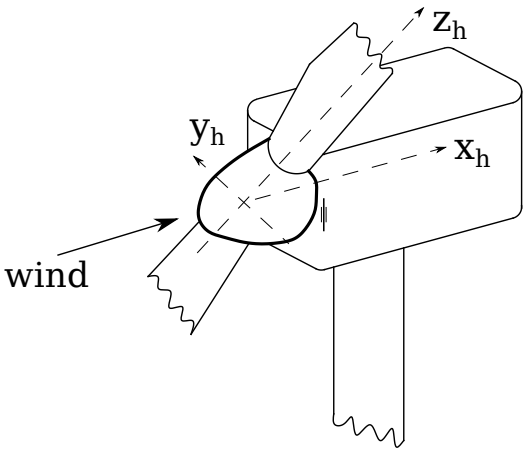

Figure 2.2: The hub coordinate system in accordance with the International Electrotechnical Commission (IEC) standards [1]

to misrepresention of the effects of large scale rotor deformations on the computation of aerodynamic forces, which in turn affects the deformation itself, leading to a misrepresentation of the dynamic aeroelastic interaction.

On the other hand, the novel member of the BEM model family used in this research is called the Dynamic Rotor Deformation-Blade Element Momentum model (DRD-BEM). This model accounts for the aerodynamic effects of the misalignments at every blade section. This is achieved by transforming the velocity and force vectors across different coordinate systems, from the coordinate system of the free-stream wind, to the coordinate system of the blade section. These coordinate transformations are done by a set of orthogonal matrices that account for all forms of misalignments at each instance. These include misalignments brought about by blade deformation, mechanical inputs like pitching and yawing, or even pre-conformed misalignments like pre-bending of the original blade.

Figure 2.1 shows a schematic view of the annular actuator swept by a blade element, its instantaneous position, and its span-wise length, δl, which are projected onto the hub coordinate system, h (figure 2.2). The actual area of the annular actuator swept by the blade element, defined by the radial thickness, δr_h, and the radius r_h, is constantly updated.

Here, we shall provide a brief description of the advanced technique used in the DRD-BEM approach to simulate the structural response of the blade, which is based on the Generalized Timoshenko Beam Model (GTBM). More details are available in Ponta et al. [33] and Otero and Ponta [40]. Since rotor blades have a complex structure and heterogeneous material distribution [41], it is challenging to use the classical beam theories like the standard Timoshenko Beam Model. Furthermore, blade analysis with classic beam theories can have significant errors , due to *ad hoc* kinematic assumptions. GTBM theory was developed to account for these limitation.

GTBM, a dimensional reduction method, has the same parameters as the traditional Timoshenko model and can work for complex beams that may have twisted or curved shapes. In this model, originally introduced by prof. Hodges [42, 43], the beam section does not remain planar after deformation and a 2-D finite element mesh is used to interpolate the warping of the deformed section, A mathematical formulation is used to write the 3D strain energy in terms of the classical 1-D Timoshenko model. Therefore, the complexity of the 3-D model and geometry of the blades are reduced

into a stiffness matrix for the corresponding 1-D beam which can then be solved along a reference-line, L, representing the beam's axis on the original configuration.

The GTBM technique ensures a 6×6 symmetric stiffness matrix, fully populated, instead of only 6 stiffness coefficients as in the classical Timoshenko theory. Therefore, using the GTBM technique we can decouple a 3-D nonlinear problem into a linear 2-D analysis at the cross-sections and a nonlinear 1-D unsteady beam problem which, for the aeroelastic analysis, we solve at each time step using an advanced ODE algorithm. The 2-D analysis computes the stiffness matrix and the 3-D warping functions for the equivalent beam. After the 1-D beam deformation for the ODE solution is acquired, the 3-D strains, stresses and displacements for each blade section at different time steps can be obtained using the warping functions. A new coordinate system (x_L, y_L, z_L) is introduced to represent the dynamic and kinematic variables along the reference line L, which can curve in any direction. This system follows the blade deformation into the instantaneous configuration l, becoming, x_l, y_l and z_l. Thus, the blade sections in the chord normal, chord-wise and span-wise directions stay aligned with the intrinsic system. Therefore, an accurate position tracking can be achieved by using this technique even in cases of large displacements or rotations of the blade section.

Inertia properties are also dimensionally reduced to produce a 6×6 inertia matrix for equivalent beam along the reference line L . This inertia matrix contains the moments

of inertia of both first and second order for blade sections along the span. These are acquired from a 2D integration that operates over the area of each blade section and also considers the distribution of material properties and the details of blade section shape. This matrices operate on the linear and angular velocities giving the linear and angular momentum of the vibrational motion, and the inertia forces and moments association with them. We can also calculate the inertia forces of the rotation of the main shaft and mechanisms like pitch and yaw. Therefore, all parameters such as angular, linear, centrifugal and acceleration effects are taking into account in a full 3-D representation.

The aforementioned interaction of structural and aerodynamic modules can maximize the capabilities of these advanced models. Moreover, the ODE algorithm used to integrate the structural and aerodynamics module can easily be extended to include other modules to simulate response of control systems or electromechanical devices.

The equation of motion for equivalent beam of 1-D finite element problem is solved by means of a non-linear adaptive ODE. This type of solver checks the solution by tracking the truncation error at each time step. The control system can be modeled by adding differential equations to the general ODE algorithm. This nonlinear adaptive ODE, which is used as a *common framework*, can be useful to create a way to integrate solutions of all multi-physics aspects of the problem.

A flow chart of the scheme demonstrating the interaction between different modules

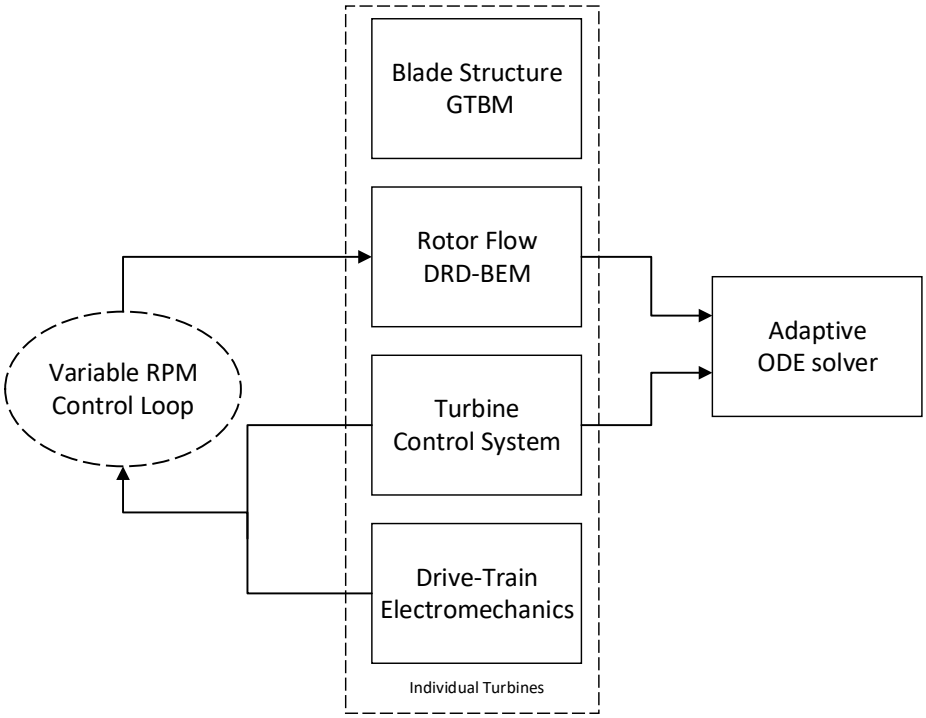

Figure 2.3: Common ODE Framework

can be seen in Figure 2.3. Modular design of a multi-physics model can help to simplify code development by improving each submodel independently. Therefore, analysis of the aeroelastic problem and innovative control strategies including mechanical and electrical aspects, can be done at the same time by using an integral computationally efficient solution through a self-adaptive algorithm.

2.1 Summary of the DRD-BEM algorithmic structure

First we consider the velocity vector of the flow aligned with the hub coordinate system h (the flow through an annular actuator). Its components are affected by the axial induction factor, a, which represents a decrease in the axial velocity across the actuator and the tangential induction factor, a', representing an increase in tangential velocity across the actuator.

$$\mathbf{W}_h = \begin{bmatrix} W_{\infty h_x}(1-a) \\ W_{\infty h_y} + \Omega\, r_h a' \\ W_{\infty h_z} \end{bmatrix}, \tag{2.1}$$

Equation 2.1 shows the velocity vector of wind that is going through the annular actuator. $\mathbf{W}_{\infty h}$ is the undistributed wind velocity in h coordinate system, Ω is the angular velocity of the rotor, and r_h is instantaneous radial distance (see figure 2.1). These three components of $\mathbf{W}_h$ show that stream-tubes associated with the blades element are aligned with the wind direction in h system. Then, the forces applied by the annular actuator will change the path of flow particles and consequently, alter the path of the stream-tubes as well. The three dimensional $\mathbf{W}_{\infty h}$, takes into

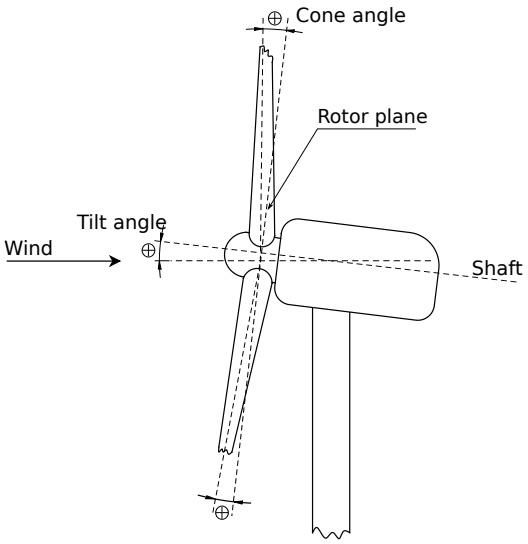

Figure 2.4: Cone angle θ_{cn} and tilt angle θ_{tlt} for upwind turbines, as given by the International Electrotechnical Commission (IEC) standards [1]

account the wind direction or yaw angle changes by means of a set of orthogonal matrices that transform $\mathbf{W}_{\infty wind}$ into $\mathbf{W}_{\infty h}$. Here $\mathbf{W}_{\infty wind}$ represents the undisturbed wind velocity in a coordinate system aligned with the wind. The tilting matrix, $\mathbf{C}_{\theta_{tlt}}$, as defined by IEC standards [1], accounts for the vertical misalignment around the horizontal axis of the nacelle system (figure 2.4). The azimuthal orthogonal matrix, $\mathbf{C}_{\theta_{az}}$, transforms wind velocity into hub system by rotating the blade around main shaft to its instantaneous position. The orthogonal matrix, $\mathbf{C}_{\Delta\theta_{yaw}}$, considers misalignment between nacelle orientation and wind direction.

$$\mathbf{C}_{\Delta\theta_{yaw}} = \begin{bmatrix} \cos(-\Delta\theta_{yaw}) & \sin(-\Delta\theta_{yaw}) & 0 \\ -\sin(-\Delta\theta_{yaw}) & \cos(-\Delta\theta_{yaw}) & 0 \\ 0 & 0 & 1 \end{bmatrix}, \tag{2.2}$$

where $\Delta\theta_{yaw}$ is the difference of the direction between incoming wind direction and the nacelle orientation. The negative sign is due to positive definition of the *TS 61400-13 EIC:2001* for the $\Delta\theta_{yaw}$.

These matrices transform $\mathbf{W}_{\infty wind}$ to $\mathbf{W}_{\infty h}$:

$$\mathbf{W}_{\infty h} = \left(\mathbf{C}_{\theta_{az}}\mathbf{C}_{\theta_{tlt}}\mathbf{C}_{\Delta\theta_{yaw}}\mathbf{W}_{\infty wind}\right). \tag{2.3}$$

$\mathbf{W}_h$ goes through more coordinate system transformation from hub coordinate system to the system aligned with the blade section. First, matrix $\mathbf{C}_{\theta_{cn}}$, considers the coning angle for the rotor, which could be either a fixed angle (like NREL 5MW reference wind turbine [32]) or a variable matrix that control performance in real time. For a detailed description of the concept of coning rotors see Crawford [37], Jamieson [44], Crawford and Platts [45]. Next is the pitching transformation matrix, $\mathbf{C}_{\theta_p}$, which takes into account the pitching angle and is associated with the rotation around the pitch axis of the blade.

$$\mathbf{C}_{\theta_\mathbf{p}} = \begin{bmatrix} \cos(-\theta_p) & \sin(-\theta_p) & 0 \\ -\sin(-\theta_p) & \cos(-\theta_p) & 0 \\ 0 & 0 & 1 \end{bmatrix}, \tag{2.4}$$

As we showed in chapter 1, pitch angle at each section shows by θ_p, which is the summation of fixed pitch angle at the hub, θ_{p_0} and $\theta_{p_{ctrl}}$ which can be vary by the control system. As mentioned before the signs are based on IEC standards definition.

Two more transformation matrices are still needed. The first set is based on geometrical alignment of the blade sections at the time when the blades were manufactured such as pre-bending. $\mathbf{C}_{Lb}$ takes into account these characteristic for each position along the L . The next orthogonal matrix,$\mathbf{C}_{lL}$, comes from the kinematic equation solution of the structural model, which takes into account the instantaneous deformation of each blade section. After applying all of these orthogonal matrices,velocity vector $\mathbf{W}_h$ is now represented in the coordinate system of the blade section. Then two other parameters are added, $\mathbf{v}_{str}$ and $\mathbf{v}_{mech}$, which are blade section vibrational velocities coming from structural model and the motion of the blade section caused by mechanical devices (such as yaw, azimuth, pitch). Both of these parameters are already in the l coordinate system so the wind velocity relative to the blade section, $\mathbf{W}_l$ is:

$$\mathbf{W}_l = \left(\mathbf{C}_{lL}\mathbf{C}_{Lb}\mathbf{C}_{\theta_p}\mathbf{C}_{\theta_{cn}}\mathbf{W}_h\right) + \mathbf{v}_{str} + \mathbf{v}_{mech}. \tag{2.5}$$

As explained in the introduction, lift and drag forces per unit length of span can be found by use of magnitude of this relative wind velocity (2.6), $W_{rel} = \sqrt{W_{l_x}^2 + W_{l_y}^2}$,

and angle of attack, α.

$$dF_{lift} = \frac{1}{2}\rho\, C_l\, W_{rel}^2\, c\,, \qquad dF_{drag} = \frac{1}{2}\rho\, C_d\, W_{rel}^2\, c, \tag{2.6}$$

where as explianed in Chapter1 C_l and C_d where the lift coefficient, C_l, and drag coefficient, C_d, depend on the airfoil profile and the angle of attack, α, c is the chord length, ρ is the air density, and W_{rel} is the velocity of the incoming flow. This eventually gives us the aerodynamic load on the blade element as:

$$\delta\mathbf{F}_{rel} = \begin{bmatrix} dF_{lift} \\ dF_{drag} \\ 0 \end{bmatrix} \delta l, \tag{2.7}$$

$\delta\mathbf{F}_{rel}$ can be transformed back to the h coordinate system using the inverse of the same orthogonal matrices. Since the inverse and transpose of orthogonal matrices are same,the load $\delta\mathbf{F}_{rel}$ on the blade element in h coordinate system is:

$$\delta\mathbf{F}_h = \mathbf{C}_{\theta_{cn}}^T \mathbf{C}_{\theta_p}^T \mathbf{C}_{Lb}^T \mathbf{C}_{lL}^T \mathbf{C}_{Lthal}\, \mathbf{dF}_{rel}\, \delta l, \tag{2.8}$$

In equation 2.8, $\mathbf{C}_{Lthal}$ is the matrix that projects lift and drag forces onto the blades

section's chord-wise and chord-normal direction, aligned with the coordinate system l.

Based on Equation 2.7, since:

$$\delta \mathbf{F}_h = \begin{bmatrix} \delta F_{h_x} \\ \delta F_{h_y} \\ \delta F_{h_z} \end{bmatrix} = \begin{bmatrix} dF_{h_x} \\ dF_{h_y} \\ dF_{h_z} \end{bmatrix} \delta l, \tag{2.9}$$

where $\mathbf{dF}_h = \mathbf{C}^T_{\theta_{cn}} \mathbf{C}^T_{\theta_p} \mathbf{C}^T_{Lb} \mathbf{C}^T_{lL} \mathbf{C}_{Lthal}\, \mathbf{dF}_{rel}$, the equation 2.8 can be written as $\delta \mathbf{F}_h = \mathbf{dF}_h\, \delta l$.

In this step, each force component of $\delta \mathbf{F}_h$ from blade elements theory is equated to the change of momentum through the corresponding annular actuator.

δF_{h_x}, normal to the annular actuator, is equal to the change in momentum on $W_{\infty h_x}$ associated with axial interference factor a (equation 2.1)and δF_{h_y}, the tangential component, is equal to the change in the momentum on $W_{\infty h_y}$ associated with tangential induction factor a'. Once the solution for a and a' in the previous steps has converged, we can calculate the aerodynamic forces on each blade section. Equation 2.10 and equation 2.11 shows the calculation of dF_{h_x} and dF_{h_y}.

$$dF_{h_x} = f_{th} \frac{4\pi\,\rho\,r_h}{B} \left(W_{\infty h_x}^2\, a\,(1-a) + (a'\Omega\,r_h)^2 \right) \frac{\delta r_h}{\delta l}, \tag{2.10}$$

$$dF_{h_y} = f_{th}\, \frac{4\pi\,\rho\,r_h}{B}\, |W_{\infty h_x}|\,(1-a)\,(\Omega\,r_h)\,a'\, \frac{\delta r_h}{\delta l}. \tag{2.11}$$

In these equations, f_{th} show the loss factor of tip and hub, and B is the number of blades. $\frac{\delta r_h}{\delta l}$ transforms δl into δr_h coordinate system using the orthogonal matrices which we have already talked. $(a'\Omega\,r_h)^2$ term takes into account the actuator pressure drop, for more information see [33].

Since a and a' are unknown in equations (2.10) and (2.11), these equations are solved by using an initial guess value for each blade element.

After finding the a and a', by repeating the $\mathbf{dF}_{rel}$ calculation, we can find the aerodynamic forces by transfer it into l coordinate system by using this equation :

$$\mathbf{dF}_l = \mathbf{C}_{Lthal}\, \mathbf{dF}_{rel} \tag{2.12}$$

A detailed description of the implementation of the DRD-BEM model can be found in Ponta et al. [33] and the references therein. Menon and Ponta [46] reports results of the DRD-BEM applied to the analysis of the aeroelastic dynamics of rotors undergoing

rapid pitch-control actions, and Otero and Ponta [47] uses the model to analyze the effects of blade-section misalignment on rotor cyclic loads. Ponta et al. [33] and Otero and Ponta [40] contain the details of the structural model. Additionally, Ponta et al. [33] also includes results of the DRD-BEM model applied to the analysis of vibrational modes of composite laminated wind-turbine blades, together with validation results against the works of Jonkman et al. [32] and Xudong et al. [48].

Chapter 3

Preliminary Results

3.1 The relation between the rotor's aeroelastic response and the stall-control technique

This preliminary stage of the research plan investigated the aeroselastic behavior of the stall-controlled VSWT rotors, study the frequency content and time evolution of their oscillatory behavior, and gain a better understanding of the underlying physics. This called for a wide range of experiments that assess the effects of rapid variations on the rotor's operational conditions, like sudden gusts. To systematize this analysis, various gust conditions tested for different wind speeds. These are represented by pulses of different intensity, occurring suddenly in an otherwise constant wind

regime. These allowed us to observe the pure aeroelastic dynamics of the rotor's response.Results has been shown here to represent line of research.

In analyzing results from these experiments, we considered the evolution of several global parameters of the rotor like power, thrust and blade-tip deflection, and local parameters at particular sections along the blade span like angle of incidence, angle of attack, aerodynamic forces, torsional and bending deformations, interference factors, and vibrational velocities. Of all these parameters, we particularly focus on the angle of attack α at 90% of the span as the main observable to study, for the following reasons:

Wind turbine blades are complex structures akin to twisted beams, with airfoil-profile cross sections that vary in their twist angle, sectional shape, and chord length, from the root to the tip. As a result, the aerodynamic loads and the associated structural loads are different throughout the span of the blade. However, these changes in aerodynamic behavior throughout the blade span follow a similar qualitative pattern, resulting in a global change in behavior that, when integrated along the whole span, produces a consistent control action.

Thus, studying the aeroelastic behavior at one particular section is representative of the qualitative dynamics of the entire blade and provides insights into the main physical mechanisms responsible for that dynamics. In any wind-turbine blade, the

sections closer to the tip are designed to be more aerodynamically efficient and contribute more to the driving torque which contributes to power production. Measuring aeroelastic observable properties in these span sections is an effective way to understand the rotor response. Selecting the 90% span section for analysis is convenient as it promises to show intense vibrational and deformational effects (as close as possible to the tip), but still avoid any tip effects. This effectively takes into account the combined dynamics of the structural and aerodynamic effects on the blade.

On the other hand, the aerodynamic forces acting on the blade directly depend on the angle of attack, α, which makes it a key observable for assessing the blade loads. This property also reflects the characteristics of the rotor resulting from both geometrical alterations due to dynamic deformations and the kinematics changes of the flow due to the operation of the machine itself as a mechanism. Hence, in a complex dynamic system like this, with coupled aeroelastic modes of operation, the angle of attack could be seen as a measurable property that serves as a nexus between the geometrical/kinematic aspect of the problem and the dynamic one.

In analyzing the dynamic response of the rotor blades, it is important to note that the frequency content of the coupled aeroelastic system is different from what one would see either in a purely structural problem or in a purely aerodynamic problem were only the vortex-shedding frequencies are considered. The frequency content of the oscillatory response may include several additional frequencies of a harmonic and

quasi-periodic nature (i.e., frequencies that are not multiples of the fundamental). This frequency content, representing different modes of deformation and aeroelastic interaction, may also evolve with time after the impulse event that induces the oscillation passes. Given that the system could feed on the energy of the wind flow, this coupled response may also show attenuation of the oscillation amplitude, or to amplified oscillations leading to an increase in important structural parameters like deformation and thrust, which could eventually lead to blade damage due to either instantaneous peak-loads, or to fatigue accumulation. The first steps in the effort to exploring control strategies to suppress these observed amplifications involves identifying operational conditions that may lead to them, and characterizing the associated frequency patterns.

In Chapter 4 you can see the results for the time evolution of the displacement in a section at 90% of the blade span, for the DU-5MW alternative Stall-Controlled RWT operating in a variable speed mode at different wind conditions above the nominal (i.e., for each wind speed, the rotor is turning at a rotational speed which ensures its power output is limited to the nominal power of the drive-train). The test shown introduces a short pulse in wind-speed representing the occurrence of a gust, and the further oscillation of the displacement, around its original constant value at each one of the operational conditions. Chapter 4 show three different responses of the rotor dynamics in more detail, which allow us to identify a threshold value in the wind speed at which we have attenuation or amplification of the oscillation induced by the gust.

Bellow this threshold, the energy of the oscillation mostly comes from the gust itself, and the system dissipates it by aeroelastic dampening. Above the threshold, after the gust triggers the oscillation the system feeds on the kinetic energy of the wind flow, and exhibits aeroelastic amplification. We are going to explain these behavior more in detial in chapter 4 and chapter 5.

Chapter 5 illustrates the characteristic frequency content of the evolution at the threshold itself. This is typical of threshold conditions that we have observed in our experiments, which show the fundamental frequency, plus harmonic and quasi-periodic components. This frequency richness exhibited at the threshold encompasses several forms of oscillatory behavior spread over the timespan of the simulation (for more detail about frequency contain can be found in [49]).

3.2 Additional considerations about the stall condition along the blade span

A further step in the analysis of the aeroelastic stability of the rotor aims at understanding the underlying physics that govern the behavior of some key parameters, which could be used to adopt critical design decisions. We shall attempt to connect the observations made on the oscillatory behavior, with the distribution of flow and structural parameters over several airfoil sections along the span. As it was mentioned

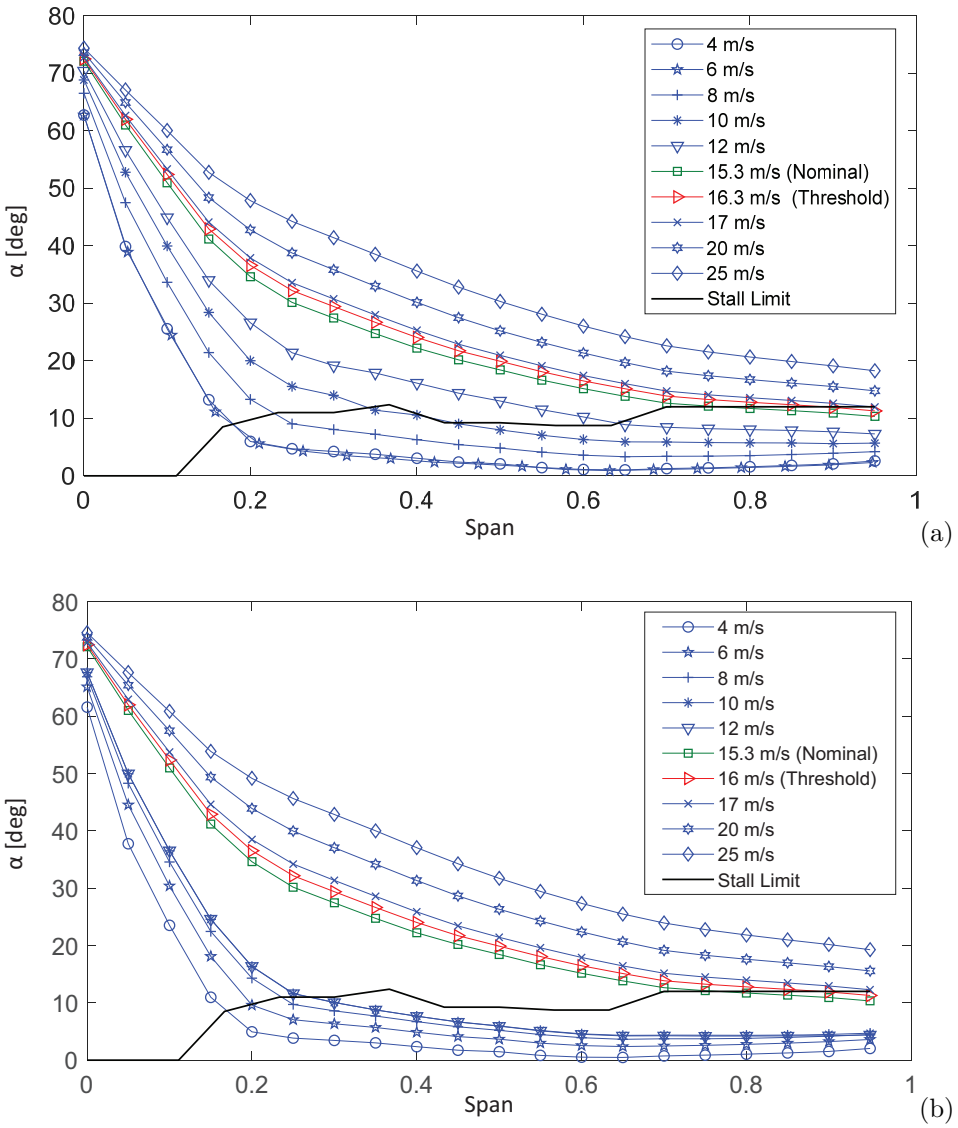

Figure 3.1: Distribution of α along the span of a DU-5M RWT blade at different wind-speeds, operating in its original FS stall mode (a), and in a VS stall alternative (b).

before, one of the most important indicators in terms of defining blade dynamics is the angle of attack, α, whose span distribution can help us to understand which factors trigger a certain response of a blade under different operational conditions.

Figure 3.1 shows the distribution of α along the span of a DU-5M RWT blade at

different wind-speeds, operating in its original fixed speed stall mode, figure 3.1(a), and in a variable speed stall alternative, figure 3.1(b). The black curve in both plots indicates the values of α for the stall transition for each section along the span (i.e., the limit of the attached regime). The α stall limit depends exclusively on the type of airfoil profile of the blade section, so it is an intrinsic property of the blade geometrical design that does not change with operational conditions. A particular advantage of these plots in figure 3.1 is that they allow us to immediately identify, for every single operational condition, which regions of the blade span are in attached regime (those where α is below the stall limit), which are in stall, and also the position of the transition between the two aerodynamic regimes (the point where the α curve intersects the stall limit curve).

One of the first things that could be noted by observing the differences between the two plots is the shift of the α curves, from the original fixed speed mode to the variable speed one, for operational conditions of wind-speeds below the nominal value of 15.3 m/s. For the variable speed turbine, we see the curves *piling-up* towards the lower end of the plot. This is a consequence of the increase in rpm, which increases the tangential component of the relative velocity $r\Omega(1+a')$, and then reduces the angle of incidence φ, and thus, α (see figure 1.2, and the associated discussion in chapter 1). This effectively produces a *de-stalling* of the inner sections of the blade, as now those α curves cross the stall limit (black curve) at a point closer to the blade root. This means that a much larger portion of the blade span is now operating in an attached-flow

regime, which leads to an increase in the driving torque, and thus, power generation. These cases correspond to the operational regimes that renders the increase in power-conversion efficiency indicated in the red-shaded zone in figure 1.6(b).

By reducing the rpm for wind speeds above the nominal, VS stall control allows us to flatten the power curve of the machine into a plateau set at the nominal power, thus avoiding extra loads on the drive train. This is symbolized by the blue-shaded area in figure 1.6(b). The effect on the α distribution is not so marked as in the case of wind speeds below the nominal, as the change in rpm needed to exert the power-limiting control action is more subtle, and the shift in the curves is relatively small.

There is a very interesting fact that we noticed in these sets of experiments that could substantially help shed light on the underlying physics of the stability threshold: Even the relatively small change in rotational speed required to adjust the power output in variable speed stall mode (from the 10.7 rpm of the original fixed speed mode to 10.58 rpm of the variable speed), produces a change in the stability threshold in wind speed. As it was seen, for VS mode operation, the threshold occurs approximately at 16 m/s, but for the same rotor design (with identical aerodynamic shape) operating in FS stall mode, the threshold occurs at 16.3 m/s. However, we also noticed that, even though both operational parameters, wind speed and rotational speed, have changed, the α distribution curve at the stability threshold (shown in red on both panels of figure 3.1) remain practically unaltered. It seems that this α distribution

curve represents a signature parameter for the stability limit. To further explore this hypothesis, we extended our experiments to include other regimes combining different values of wind and rotational speeds. In all the cases studied, the α distribution curve for the stability threshold condition was practically identical, confirming the aforementioned notion that the α distribution along the blade span is a key parameter in determining the stability transition.

Figure 3.2(a) shows some examples of α curves results from these tests at the threshold condition, including the α curves shown in red in figures 3.1(a) and 3.1(b), and extreme cases with rotational speeds well above and below the nominal, like 8 rpm or 15 rpm. As could be seen, all the threshold curves practically coincide, regardless of the disparity of the combination of wind and angular speeds. This is a remarkable feature given the fact that many aerodynamic and structural variables change when the operational conditions depart from the standard values. We should recall that the aeroelastic response is a highly non-linear phenomenon, and large changes in the rpm and wind speed, lead to large changes in the interference factors (which affects the vectorial composition of the relative velocity, and its incidence angle φ), and also the torsional deformation (which affects the twist, and hence the pitch angle of each blade section θ_P). Both aspects are essential in the determination of α (see figure 1.2, and the associated discussion in chapter 1). Nevertheless, in spite of all the differences in the whole set of parameters governing the problem, the distribution of α at the stability threshold remains the same. Because of its richness, this is a topic

for for a further paper where we intend to analyze several alternative blade designs in order to further explore the role of α distribution along the span, using the gained physical understanding to create advanced blade geometries for VS stall operation that exhibit improved stability and performance.

Another interesting aspect to notice on these preliminary experiments is that the point along the span marking the transition between the stalled region on the inner blade, and the attached region on the outer blade, has moved beyond the 90% the span when the stability threshold occurs (see the crossing point of the α and the stall-limit curves in figure 3.2(a)). Looking at the blade planar shape depicted on figure 3.2(b), we could see that beyond 90%, the distribution of cord-length of the airfoil sections rapidly decreases following an elliptical profile, which *terminates* the blade shape reducing the chord length to mitigate the effect of tip vortices. This essentially means that the blade is aerodynamically productive up to about 90% of the span, beyond which, its contribution to the generation of aerodynamic loads diminishes rapidly. As it was mentioned in chapter 1 in reference of the way in which the stall control method works, the possibility of allowing the attach-to-stall transition point to gradually move along the span is critical for the smooth operation of the stall control method. That is, it could be said that the 90% position marks the end of the aerodynamic smooth control functionality of the stall technique. Essentially, all the blade is already in stall, and the changes in aerodynamic loads become more abrupt. This can make the blade more susceptible to experience unstable oscillations triggered

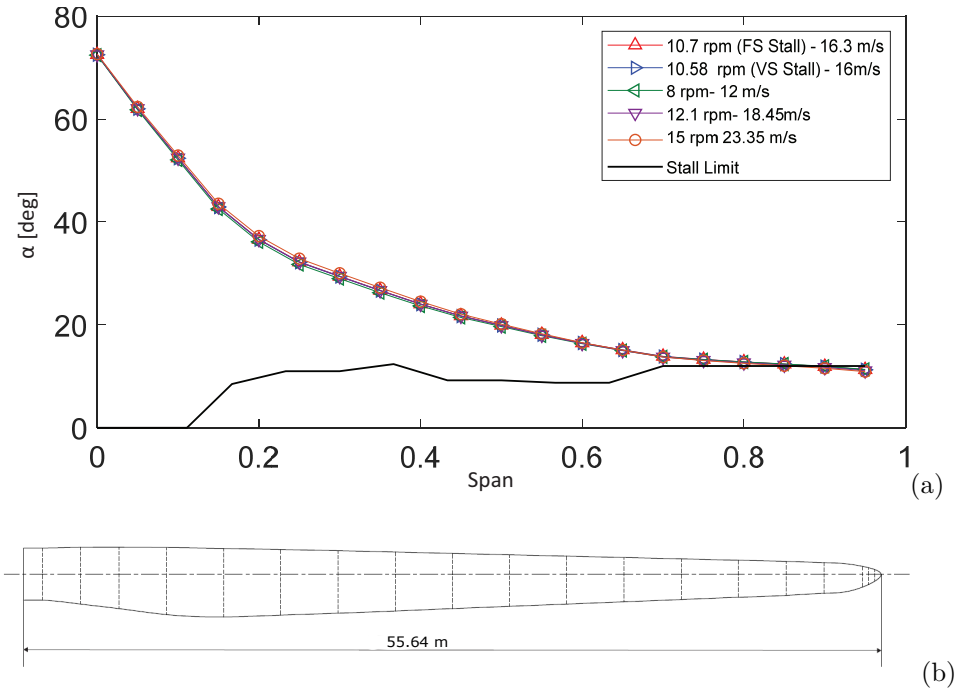

Figure 3.2: ((a): Examples of α distribution curves from tests at the wind-speed threshold condition. (b): Planar shape of the DU-5MW RWT blade.

by sudden changes in operational conditions like the impulsive gusts in the examples presented. This is another aspect of the underlying physics that we intend to explore in the proposed research plan.

Chapter 4

Analysis of Wind Fluctuations in Terms of their Effects on the Dynamic Response of the Rotor

In this chapter, we begin with a characterization of the gusts and the turbulent atmospheric fluctuations. Subsequently, we shall introduce the three different behaviors of the rotor observed at different wind speeds for the same pulse characteristics. In the next chapter we present a detailed analyses of the different behaviors, the energy transfer correlation and the reduced order characterization.

4.1 An Examination of Atmospheric Flow Data

Frequency filters were applied to publicly available wind measurement datasets, found in [2, 3], to isolate, identify, and quantify the gusts with a characteristic time span around a certain δt and then measured their average amplitude. Figure 4.1 shows a sample of a frequency filter applied to one of the wind measurement datasets.

4.2 Pulse characterization map

In this section we shall be discuss the characterization of the wind pulses that were identified as mentioned earlier. Figure 4.2 shows the different pulses that were identified from various datasets.

Characterization of these pulses is imperative to better understand their effects on the system. The first group of pulses is the region bound within the time span upto 0.25s and the amplitude of 1m/s . This region consists of pulses which can be attributed to turbulent fluctuations in the wind. The next group is one which we refer to as the wind "gusts" - pulses with time spans of 1 to 3s and amplitudes between 1 to 3m/s. The region of pulses just below this, the one with the same time span of 1 to 3s but with amplitudes lesser than 1m/s correspond to a gradual increase in wind speed and

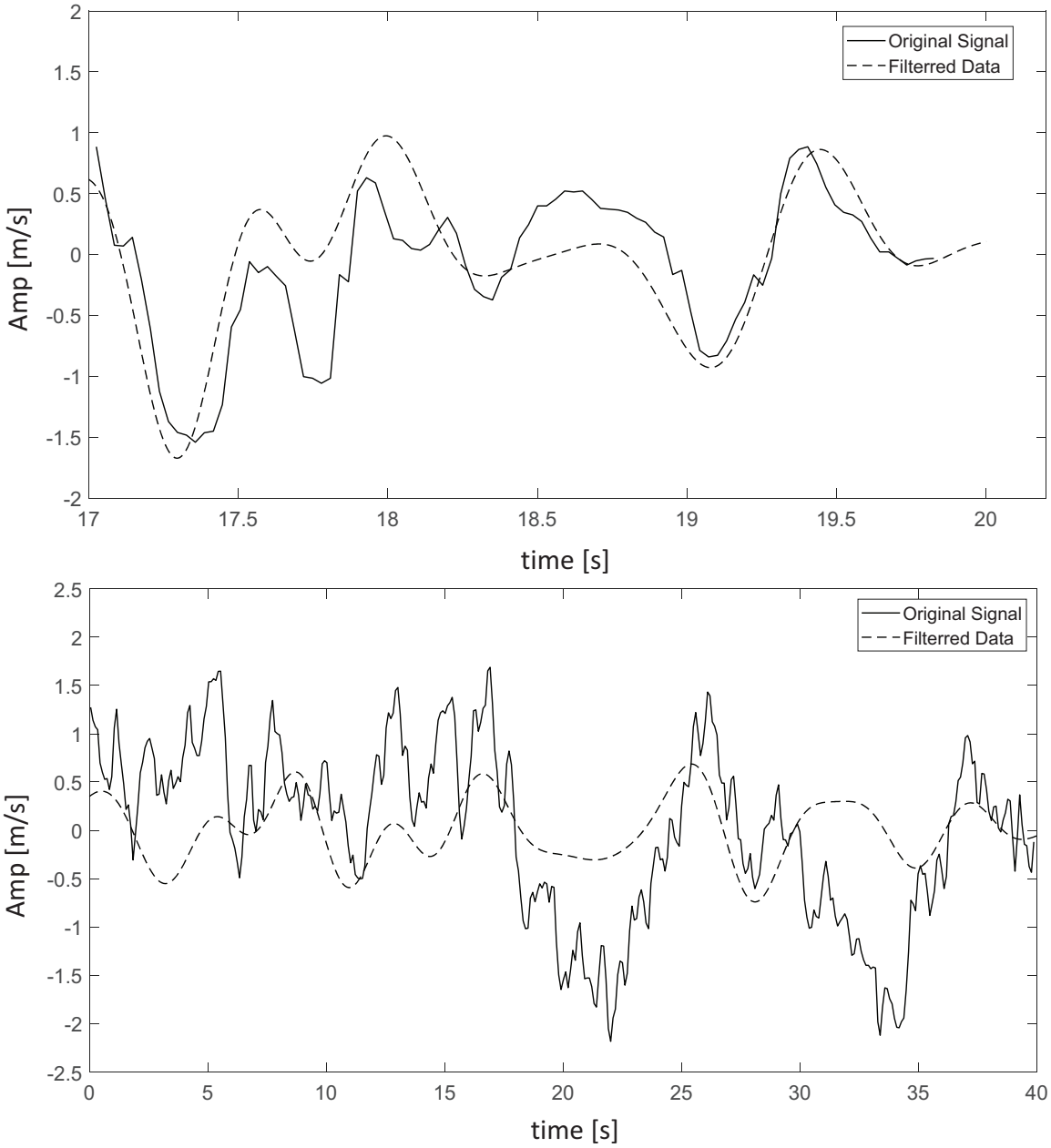

Figure 4.1: Sample of real and filtered data[2, 3]

as such do not lead to any observed oscillations in the system. For pulses of this region, because of the longer duration of the pulses, the system has enough time to adapt itself due to its inertia without any oscillations/unstable behavior. Pulses with

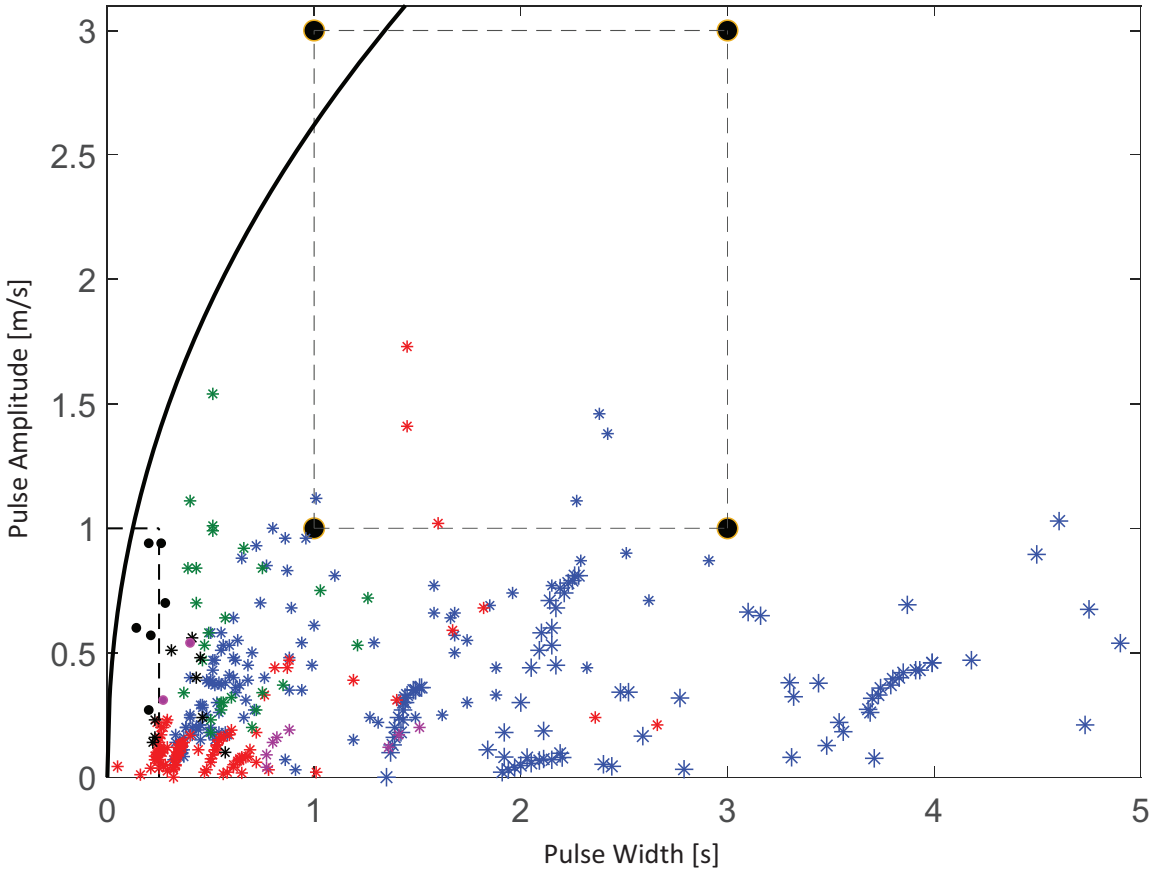

Figure 4.2: Pulse Characterization Map

a short time span of upto 0.25s and magnitude upwards of 1m/s are extremely sharp variations. We have been unable to observe any wind measurement data indicative of any these wind states and hence it is reasonable to consider these conditions to be unrealistic (or statistically significant) for any analyses/design considerations.

The intermediate region - the one with its bounds for time span from 0.25s up to 1s is once which does not demonstrate a fixed response. In this "transition zone", the energy of the pulse is not entirely transferred to the blade's elastic energy but a part of it is dissipated by aerodynamic damping of the oscillations as well. This region

does not exhibit a fixed type of response from the system. The only distinguishing indicator of the existence of the transition zone is the presence of oscillations for pulse spans near to 3s.

4.3 Different types of system responses

With fig 4.2 as a guide, we conducted several numerical experiments of varying pulse amplitudes and time spans for different wind speeds.

We observed three different responses of the system: a. A stable oscillatory regime - wherein the system's oscillations are damped and eventually it stops oscillating. b. A threshold condition - wherein the system continues to oscillate but reaches a state of fixed amplitude of oscillations. c. unstable regime - wherein, above the threshold velocity, even a small pulse leads to a continuous amplification of the system's oscillatory behavior (see Jalal, Ponta, Baruah [49]).

A sample of these behaviors is presented in figure 4.3. We shall be discussing these in detail in chapter 5. In addition to single pulses from the different regions of the pulse characterization map (Fig 4.2), we also experimented with a train of pulses. We observed that while the system was in the stable oscillatory regime, the train of pulses triggered amplifications which eventually decayed. This indicates that each of pulses

in the train only lead to a "reset" of the operating conditions and once the pulse had passed, the oscillations decayed and the blade became stable. This is especially crucial since it exhibits the limits of stability of a particular blade.

Observations of the stable oscillatory regime clearly demonstrate that the system is dissipating energy and that the energy comes from the pulse. The amplitude of oscillations scale exactly with the kinetic energy of the pulse, regardless of the value of damping. Thus, the system never absorbs any additional energy from the flow. Above the transition zone, a small pulse can trigger oscillations in the system which never decay since the system then starts absorbing energy from the flow itself. This is contrary to the behavior in the stable oscillatory regime where the system dissipates energy by oscillations damped by aerodynamic damping. This further indicates that the transition depends exclusively on the aerodynamic behavior.

If the pulse is quick enough such that all its energy is delivered to the blade before its first oscillation peaks, most of the energy is absorbed as elasto-inertial energy. To elaborate, the kinetic energy of the pulse is delivered so fast that the blade moves and expends some energy by inertia of motion and subsequently when the blade deflects, the remaining, major part of the energy of the pulse which was not expended by its inertia ends up as elastic potential energy. With pulses of longer duration, we observe that there is ample time for energy dissipation by aerodynamic damping in the duration of the pulse itself and a major portion of the energy does not end up

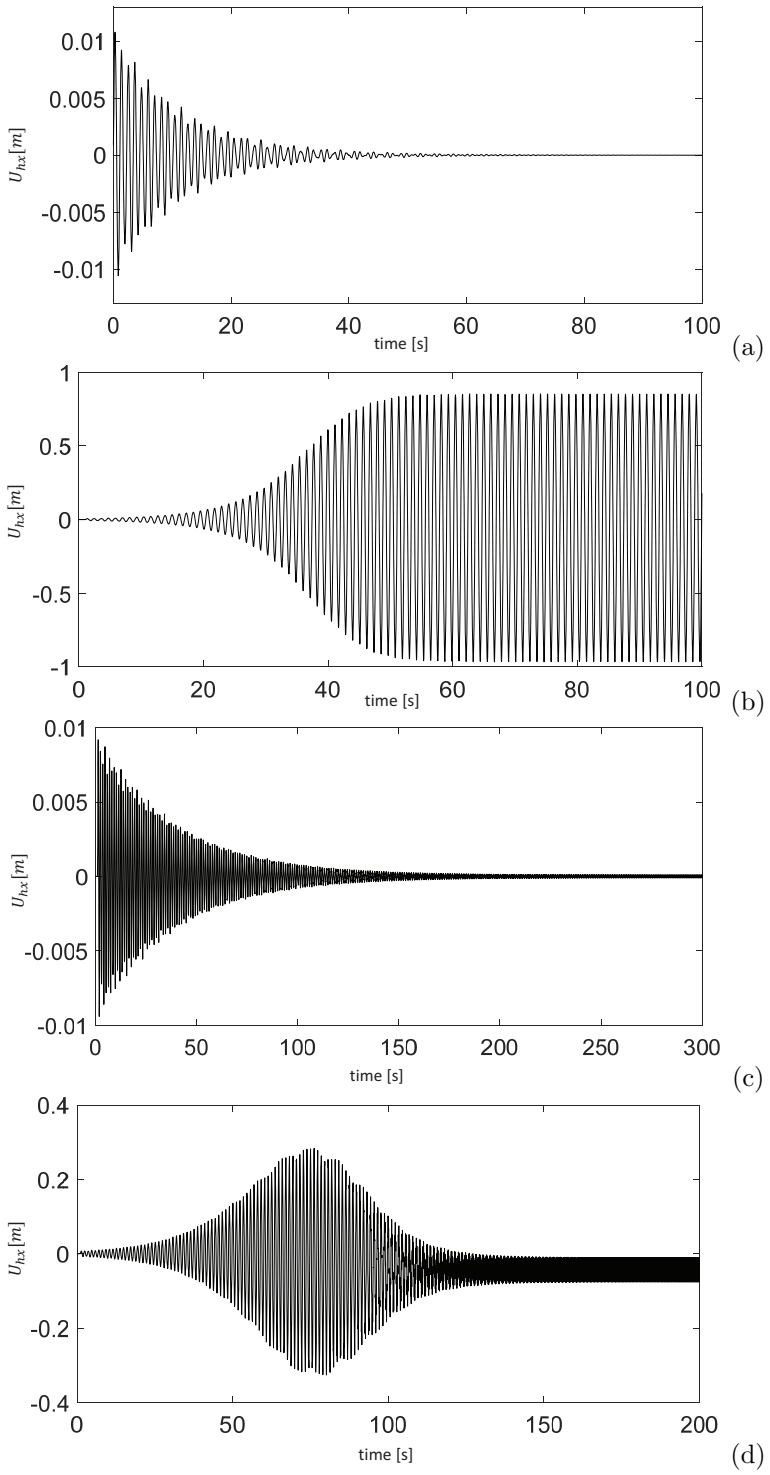

Figure 4.3: Time evolution of displacement at 90% of the blade span for the DU-5MW RWT at different wind conditions. (a): 16 m/s, (b): 17.5 m/s, (c): 16.5 m/s (d): 17 m/s

as elastic potential energy in the blade. And as such, we can no longer characterize this with the energy transfer correlation, which we shall be discussing in the following chapter.

A large flutter of the blade when it is unstable can potentially destroy it. Even for the stable oscillatory regime, repeated oscillations can accumulate to fatigue stresses that can compromise the operational life span of the blade. These are of special concern from a controls standpoint to mitigate vibrations that can lead to a long-term failure or an immediate destruction of the blade if they amplify uncontrollably. Hence the determination of the aerodynamic damping conditions is important and we shall revisit these in chapter 5)

The practical application of this study is the development of novel reduced order models for turbine rotor controls. With a reduced order model, we retain the most important aspect to characterize the oscillations and can hence create control strategies that can predict the highly non-linear, complex behavior of the system with very simple elements and react to it in real time.

Chapter 5

Numerical Study

In analyzing the dynamic response of the rotor blades, it is important to note that the frequency content of the coupled aeroelastic system is different from what one would see either in a purely structural problem or in a purely aerodynamic problem were only the vortex-shedding frequencies are considered. The frequency content of the oscillatory response may include several additional frequencies of a harmonic and quasi-periodic nature (i.e., frequencies that are not multiples of the fundamental). This frequency content, representing different modes of deformation and aeroelastic interaction, may also evolve with time after the impulse event that induces the oscillation passes. Given that the system could feed on the energy of the wind flow, this coupled response may also show attenuation of the oscillation amplitude, or to amplified oscillations leading to an increase in important structural parameters like

deformation and thrust, which could eventually lead to the blade damage due to either instantaneous peak-loads, or to fatigue accumulation. The first steps in the effort to exploring control strategies to suppress these observed amplifications involves identifying operational conditions that may lead to them, and characterizing the associated frequency patterns.

In this chapter we are going to study the results from the experiments mentioned in Chapter 4. In Section 5.1, we are going to analyze the characterization of the process of energy transfer. In Section 5.1, we are going to analyze the oscillatory behavior on the stable regime of wind speeds, where the energy of the pulse is dissipated by the aerodynamic dumping, and how this manifest itself in different manner along the range of wind speeds all the way up to the beginning of the transitional wind peed range at approximately 16.5 m/s. In Section 5.13 the the focus of the analysis is on the unstable regime, covering the range of wind speeds from 17.5 m/s all the way up to the cut-off speed of 25m/s, which is the highest operational speed of the turbine. In Section 5.1 we analyze the frequency content on the relatively narrow transitional wind-speed range between 16.5 m/s and 17.5 m/s.

5.1 Characterization of the Energy Transfer Process from the Pulse to the Rotor

In this section we will study the characterization of the energy transfer process from the kinetic energy of the gust pulse to the elastic energy accumulated by the deflection of the rotor blades.

Figure 5.1 shows 20 different cases with different pulse length and intensity, which all of them zeroed at the peak of the pulse, with 3 different incoming wind speeds. This is clear that we have an almost perfect collapse. When we have the normalization of the displacement with the energy of the pulse for each velocity, it gives one clear constant which is called $1/K_{el}$ which has the dimension of the inverse of the stiffness $(1/KN)$. This constant can be generalized for all other wind speeds as well. To continue our observation we are going to grab one case from each velocities (case with 0.5 m/s pulse intense and 0.2 seconds pulse length). For all of these cases we grab the height of the first peak of the displacement signal, because essentially when the pulse comes, turbulent fluctuation occurs so rapidly, that all the kinetic energy drop on to the blade and then it is transformed at the beginning in a mixture of inertial and kinetic energy (motion of the blade), so essentially inertial energy on the blade which is displacing and then increasing into elastic energy until it reach to the first peak with most of the

energy of the pulse became in the first order characterization , there must be some dissipation in the process but is it not remarkable and practically all that energy from the pulse goes to that first peak. This is the initial maximum value when all the energy of the pulse stored in the system as an elastic energy. Moreover it seems that $1/K_{el}$ is consistent with the notion , the $1/K_{el}$ is clearly going to increase as we go higher in wind speed and it is very consistence with the logic because the deformation of the steady state situation at the higher wind speed increases systematically with wind speed so essentially the blade is pre-stressed at the moment that the pulse arrived. So that pre-stressing increases the stiffness so $1/K_{el}$ goes up as we go to 16 m/s.

Figure 5.2 shows plots of the blade deflection re-normalized by the value of the the equivalent flexibility 1/Kel.

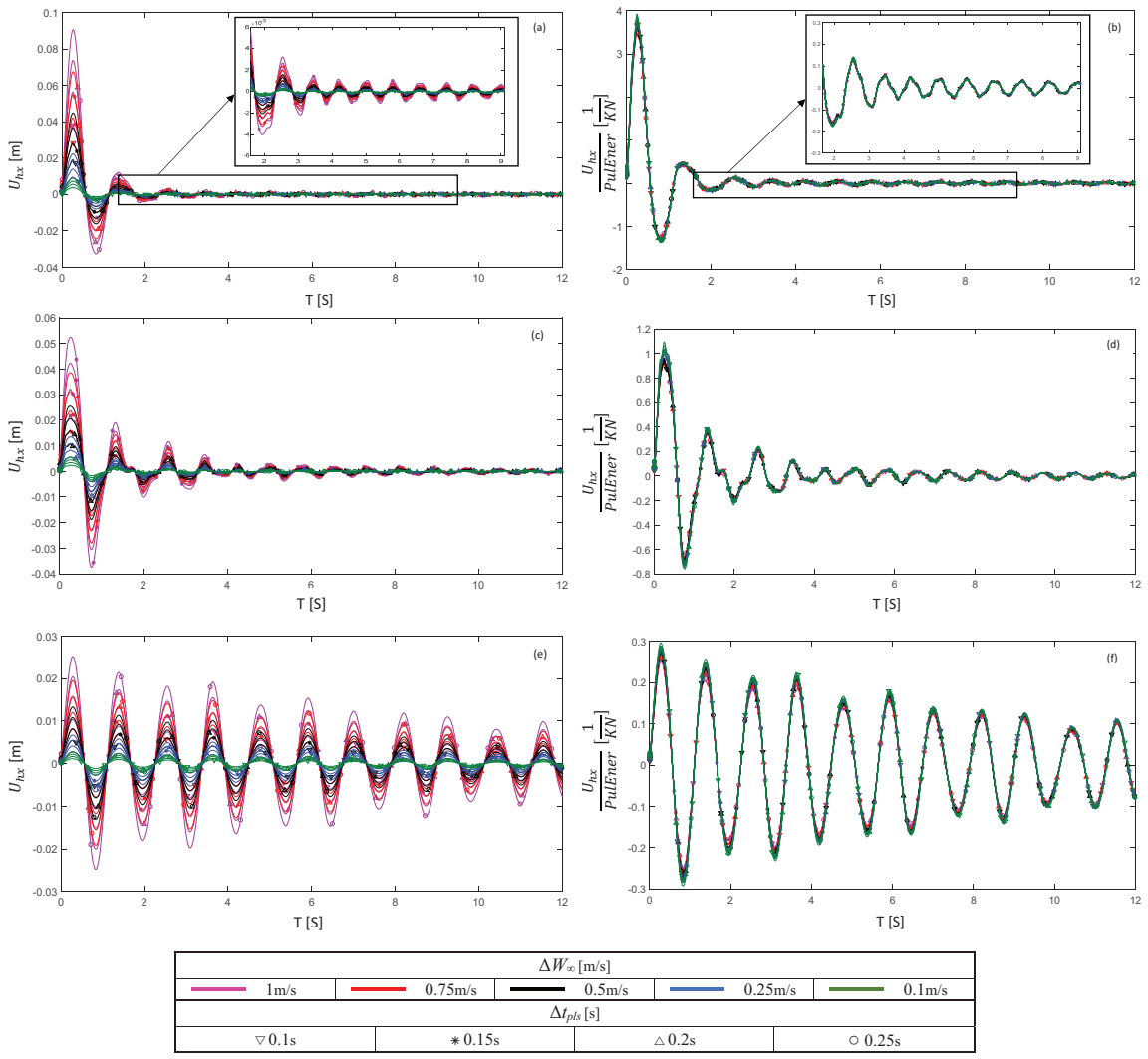

Figure 5.1: Reduction of the time evolution of the blade deflection through normalization by the kinetic energy content of the pulse for three examples of wind speeds on the stable regime: (a,b) 8 m/s; (c,d) 12 m/s; and (e,f) 16 m/s.

5.2 Reduced order characterization at the earoelastic response on the stable range of wind speeds

Now we have established that the flexibility depends on the steady state, we normalized the behavior for all of the wind speeds based on the first peak of the signals in Figure 5.2. This figure is a non dimensional quantity show the instantaneous evolution in time, each of the points of the signals is the remaining proportion of the elastic energy stays in the system in that particular time.

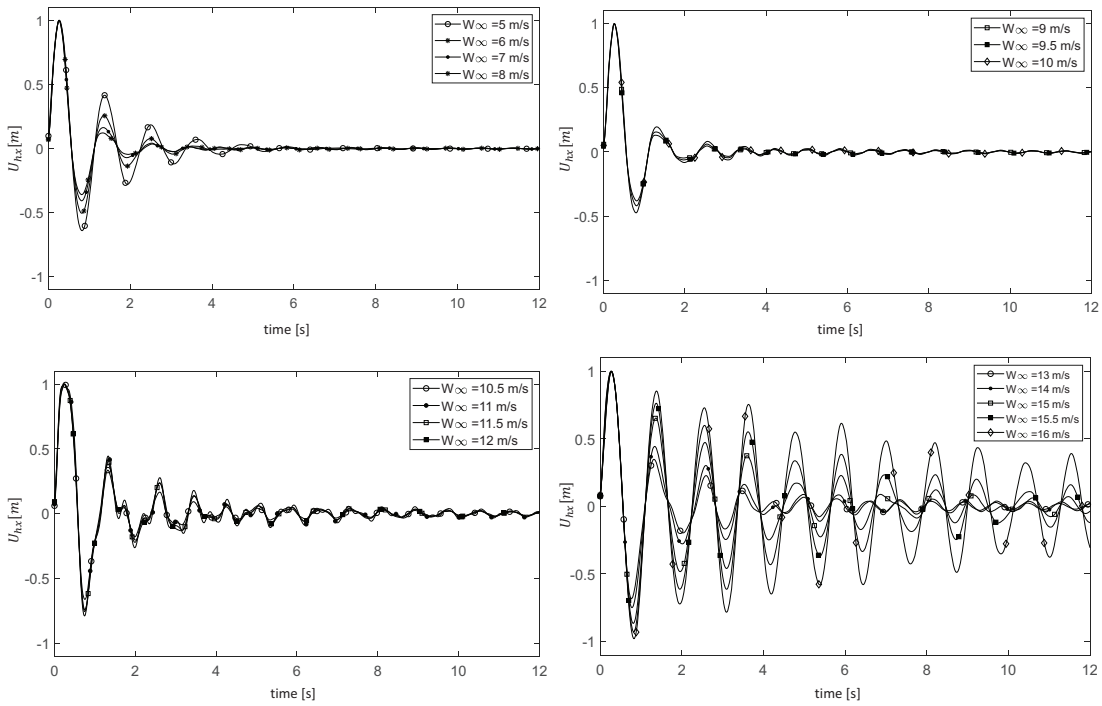

Figure 5.2: Nominalized values of blade deflection in the stable regime of wind speeds.

5.2.1 Analysis of the rate of dissipation

The remaining energy in the system at every single time step depends on the rate of the exponential decay, which could be clearly observed in the linear profiles of the enveloping curves when depicted in the semi-log plots of Figure 5.3. If λ is low, it will take longer for the energy to dissipate and if the λ is high, it indicates that the signal will dissipates quickly. Each λ also has the connection with the frequency distribution, as we have seen in short term one frequency dominates, it decay differently. λ we have

measured are associated with the typical frequency content which we are going to see in next chapter. Based on different frequency contain in each case figure 5.2 shows different groups and the λ associated to each one of these frequencies is available in figure 5.5.

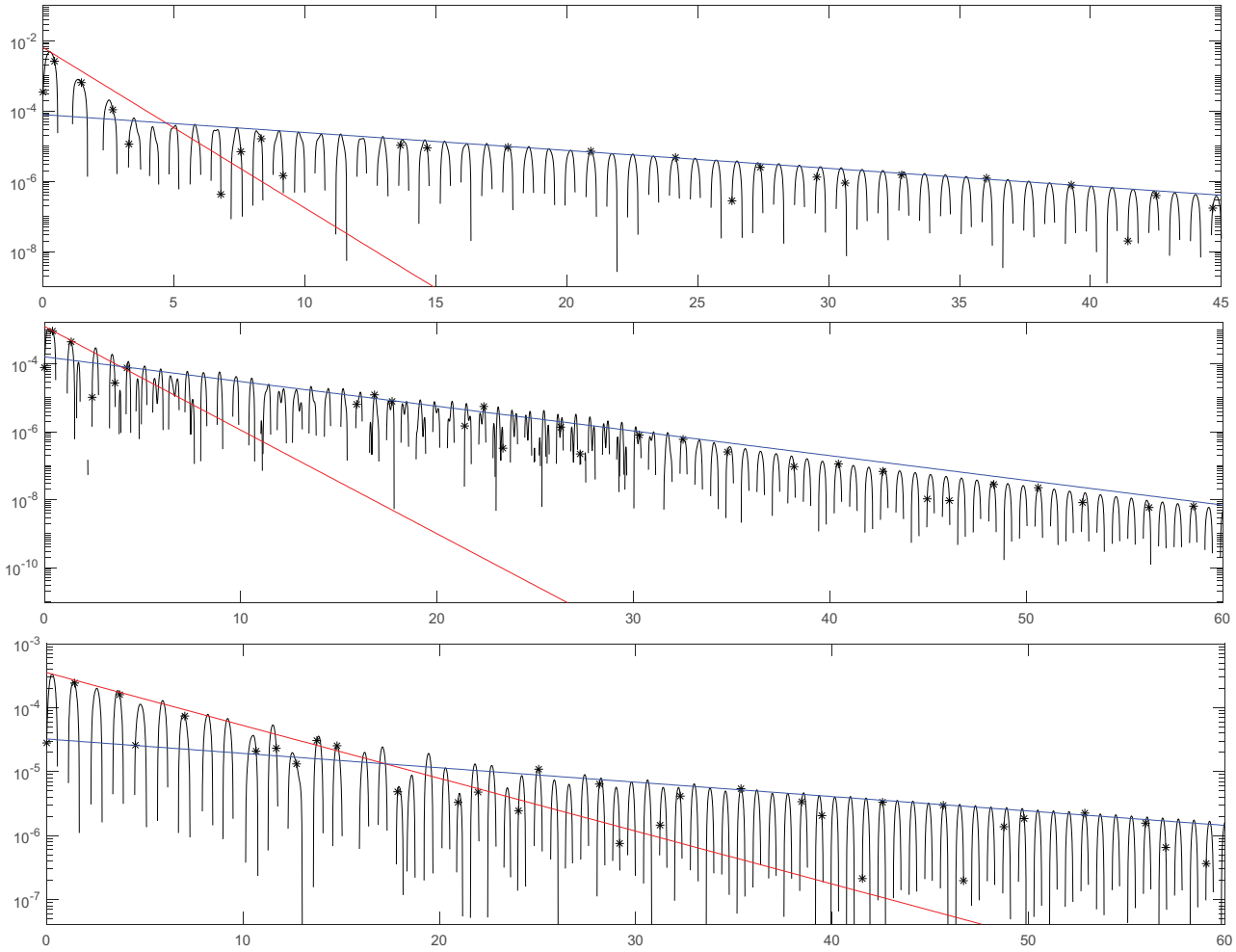

Figure 5.3: short term and long term λ in semi log coordinate

Comparing the spectra for the flexel collapsed signals, in theory the assumption is that with certain differences related with reduced order characterization, the height of the first peak of the first frequency which is one associated with the first huge decay in the energy , it collapses in proportion to the area below the exponential enveloping curve:

$$\int_0^t e^{-\lambda t}\,\mathrm{d}t$$

Therefore, here we can relate the peak associated with the first frequency, with the integral of that exponential curve according to a different λ which is super strong, because in this case we have done three different analysis, first the Energy Transfer Characterization connected with the energy of the pulse, second in prelude of stable oscillatory regime, we have connected with the elasticity of the steady state and then from elastic. Essentially we went from kinetic energy to elastic energy and then from elastic energy characterized by the steady state on which that evolution is mounted on top, so we have gone in a more universal characteristic of the system, not only many different pulses in the same velocity but many different pulses in many different velocities.

Finally we can characterize the frequency associated not only with the kinetic energy and elastic energy, but also with the rate of dissipation and that also depends on

the velocity of the wind but is different from the accumulation of the elastic energy because one thing is transferring the kinetic energy into elastic energy and another is how that elastic energy dissipates in time. So we have three passage here, kinetic energy to elastic energy and elastic energy into heat, and dissipation created by the λ , which is aerodynamic dumping.

As we have already mentioned all the signals are normalized in a way that our time starts from the peak of the gust. when we look at the signals (Figure 5.2), signals peak reach around 0.3 sec but the pulse according on this normalization is already ended in 0.1 sec, so there is a delay between the end of the pulse which is the end of the delivering of the kinetic energy from gust and when all that energy accumulated as pure elastic energy in the maximum misplacement. This happens because the energy goes to inertia of the blade in the meantime. Essentially we have kinetic energy in the wind, kinetic energy and elastic energy in the blade and finally at the peak we have pure elastic energy at the blade, that is why the peak is the natural place to go, because all that kinetic energy in the wind became finally the pure elastic energy in the blade and in the intermediate stages we have mixture of kinetic energy in the blade and elastic energy in the blade.

5.2.2 Logarithmic decay and variation of the energy method

For finding the λ we filtered the signal in order to isolate each frequency so we can focus on each frequency at once. Use used a filter and we used that to create average content of energy at that frequency to create a linear regression in the semilog which ends up to exponential in linear-linear. That is essentially another way of the numerically implementing the classical method of the logarithmic decrements, which is just finding the developing curve by just tracing those peaks even if they are contaminated with something else. This is how the filtering code works here in processing to detecting those peaks. The alternative method is that when you have functions that decays very slowly so essentially when we have the second frequency that in the long run after the elbow takes a while, that is why in the semilog plot you can see the enveloping curve as a straight line and it is very distinguishable. when you go to the first period there is a contamination of two frequencies and that is much difficult to see because besides the presents of two frequencies, first frequency is more important than the other because the decay lasts very short , that means the logarithmic decrements is very high and in those cases even though you can still measure it, it becomes difficult. The method we used to find the short term decrements is based on the energy, we grabbed the bar of the spectrum of the frequency that we wanted and using that to estimate the mean value of the exponential decay that gives the origin to that decay, the difference of these two methods is that

mean value is related with the bar of the spectrum which is originally measuring the spectral energy of that particular frequency , so it is energy equivalent method. The other one just measured the first peak. This energy based method behaves better when you have signals that decay very rapidly. If you have a perfect mathematical method any of these methods would have shown the same but when you are going to measure the real signals one works better than the other, So we suspect we are entering to the twilight zone between the first and second frequency , the second frequency is measurable by classical variation of logarithmic decrements but the short term which is associated with the decay of the first frequency λ_1 is not easy to measure in that way, so we need some sort of a energy equivalent method.

5.2.3 Analysis of frequency content

We already established at the beginning, the spectra is going from 0 to 99 second , the real dominate behavior by including those first short term cycles, is going to dominated by first frequency (λ_1).

In this regime we have discovered two stages, one is the transient at the beginning and the other is the long term behavior. We have speculated that the transient last about 5 seconds but it does not need to be a fixed number. The signal at 16 m/s started at the lower amplitude than the signal at 13 m/s and then after a while two

enveloping curves crossed and then signals at 16 m/s remained higher than the signal at 13 m/s. Essentially what we have noticed is the curve of 13 m/s starts high and then it decays rapidly and then it starts in the transient zone and then decays with the higher λ than 16 m/s but the slope is not as rapid as the transient zone, so 16 m/s seems more uniform without any distinguishable transient zone and all the time with a λ which is lower in terms of attenuation than the case of 13 m/s.

As you can see in the all wind speed there is a trend that where we do have these two time spans, the initial transient after the peak and the long term behavior. We clearly see for most of the speeds there is a clear breaking in the slope of the semi-log plot which means a change in the exponent the corresponding the logarithmic delay and there is some buffer regions in the middle when we go from one frequency dominating to the other one and we are going to establish some sort of a criteria to extrapolate those two straight lines in the semi log plot to look at the point of the intersection to clearly define these two regions of two time spans. An interesting observation is actually, both different λ and frequency are associated with time spans, essentially during the initial transient we are going to have one frequency dominating and one λ associated to it and in the long term behavior another frequency dominating and another λ associated to it.

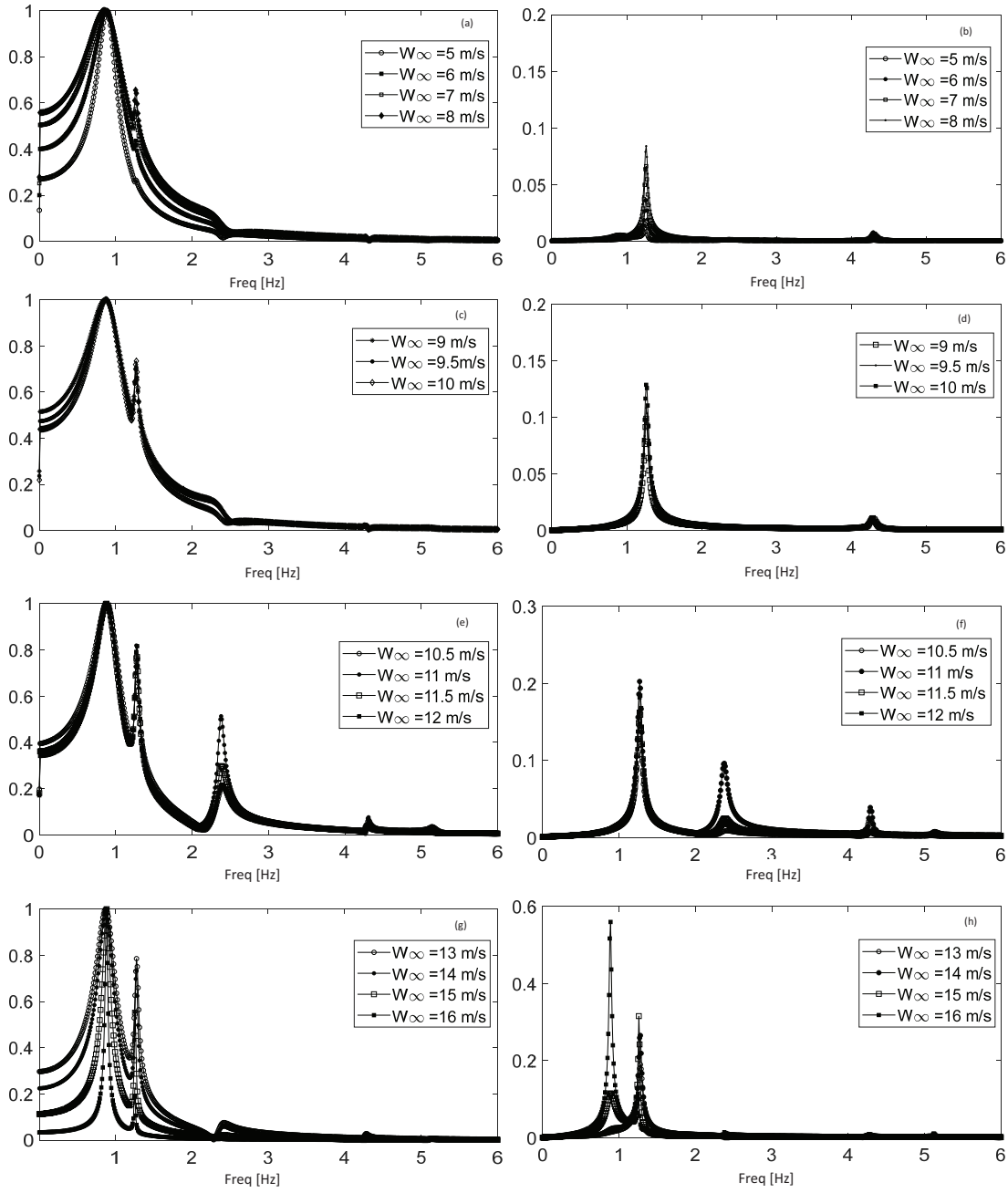

Figure 5.4: Stable oscillatory regime four Group Spectra, Right plots [0 99]sec Short term, Left plots [7 99]sec, long term

In figure 5.4, U_{hx} is the instantaneous in the axial direction (i,e, the direction parallel

with the main axes of the rotor), due to deformation, at 90% of the blade span (see Chapter 1). ΔU_{hx} is the oscillatory displacement about the constant value of U_{hx} for the deformed configuration at every value of the operational wind speed (W_∞).

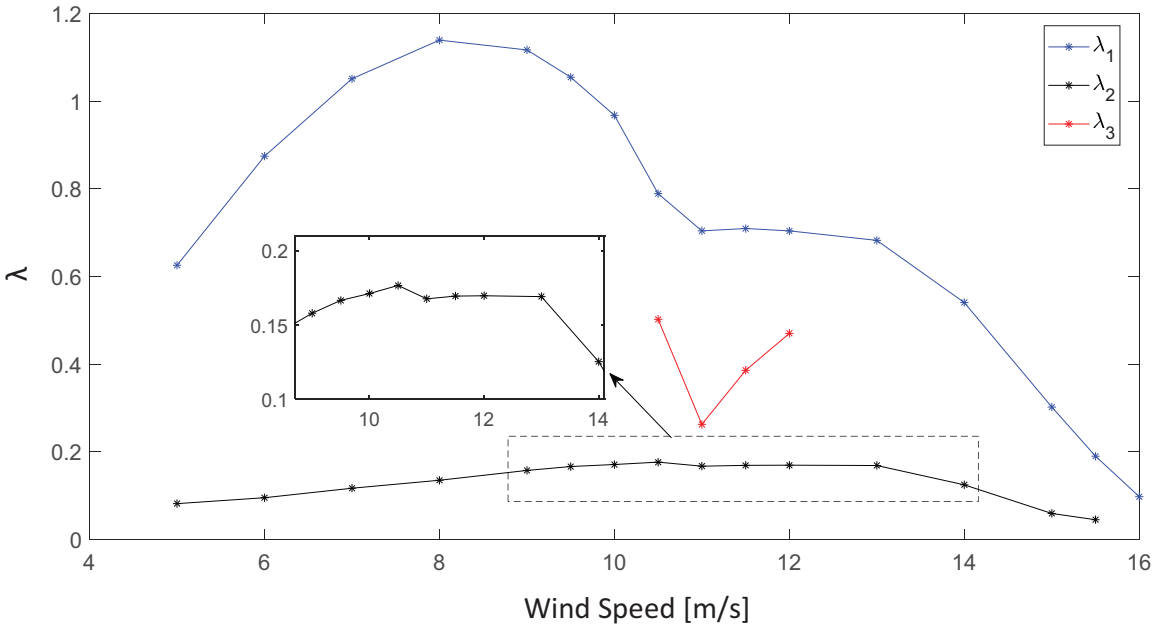

Figure 5.5: Representation of λ_1,λ_2,λ_3 in stable oscillatory regime

5.2.4 Intersection points and spectra

The idea of the transition point is going to be like the representative point in time where the system pivots from shorter behavior into the longer behavior even though that point is surrounded by a transition zone in intermediate range in time where we have a mixture of frequencies contributing and non of them are dominated. In the

cases of low speeds and high speeds during the stable region from 5-16 m/s is going to be a mostly characterized by transition from the first frequency into the second frequency and then a mixture of these two in that transitional zone. In the region in the middle associated with the 11 m/s, in additional to these two frequency, third frequency is also participating and some contribution of the fourth frequency which is very brief, but third frequency contributes to make the transitional range reacher in behavior.

5.3 Unstable Oscillatory Regime

At the unstable oscillatory regime, after the gust triggers the oscillation the system feeds on the kinetic energy of the wind flow, and exhibits aeroelastic amplification. In this region you can give a small kick and machine absorbs it and start oscillating but at the stable oscillatory regime velocities the energy that dissipated on the decaying oscillation exclusively comes from the pulse itself while at the unstable oscillatory regime the pulse trigger some absorption from the flow [49]. At the unstable oscillatory regime the pulse is an initiator and the blades start absorbing the energy from the flow which is a completely different behavior from the region at the stable oscillatory regime velocity. Because stable scillatory egime the aerodynamic direction is just damping the oscillation.

Unstable oscillatory regime can be dangerous, because even a small kick is enough to trigger the blade and make it unstable, it can take longer or if the pulse is higher the amplitude is higher.

Different energy of the pulses can affect on when the expansion start, because it could be connected to the energy of the pulse and not the ultimate amplitude, because the ultimate amplitude of the oscillation depends on the steady states velocity. we are suspect the starting point of the evolution curve can depend on the amount of energy content of the pulse.

This region is an exponential expansion that is no more than a continuation of the same exponential behavior of attenuation after crossing the transitional zone when λ become from positive to negative, and becomes an amplifying exponential so essentially it is source of energy and that energy comes from the regular unstable oscillatory regime flow. Another interesting point is the λ is very repetitive, which means regardless of the pulse it always follows a same exponential expansion so the λ in amplification zone depends exclusively on the velocity of the uniform stream.

When we are in the amplification zone, we can see different pulse configuration with different energy levels, produce a straight line in the Semilog plot with repetitive λ for each cases and at some point the exponential expansion will saturate. When we have lower energy in the pulse, the associated straight line has more time delay. That says all the curves evolve at a certain amplitude in terms of the displacement and

since it is a same blade with same deflection so it has the same elastic energy.

Here we do not know if it is because the threshold in energy or because the threshold in displacement secondary dissipative aerodynamic damping mechanism starts to play a role and since it starts with a damping even if the original λ started to be amplification, essentially it is like having a positive λ, which it competes with the λ for the unstable oscillatory regime which is negative so instead of damping it extracting energy from the flow and then it starts to grow in amplitude but the secondary mechanism is damping, so it compete with the amplification to attenuate the system and we got to the point that the two of them act together, one trying to expand the other try to attenuate to the point that they produce constant amplitude for the rest of oscillation time which this constant value depends only on velocity of the uniform stream. We have seen regardless of the pulse that we have when we have same velocity the constant value of the displacement would be the same.

In figure 5.6(a), we again ran the simulation for different pulse intense and pulse width, we can be seen that they can characterize by a expansion mechanism follow by a second mechanism that is pure dissipation and the amplitude continue expanding but at a lower rate until all the curves level at a same amplitude when both mechanism achieve an equilibrium essentially all the energy that is absorbed for the expanding by first mechanism is going to characterize by a exponential expansion which consistent with the inversion of the behavior of the behavior that we have already observed in

the chapter 4.2 but with the change of sign of the exponential decay. As we said before after the transitional zone earodynamic damping become aerodynamic amplification and the system starts to absorb the energy from free flow and increase the amount of mechanical energy absorb by the system in its oscillation until the second mechanism starts to act and the curve starts to slow down the increase of the amplitude until the all oscillation reaches a steady plateau at a constant value where both mechanism cancel each others and all the energy absorbed from the flow by first mechanism is dissipated by the energy damped by second mechanism.

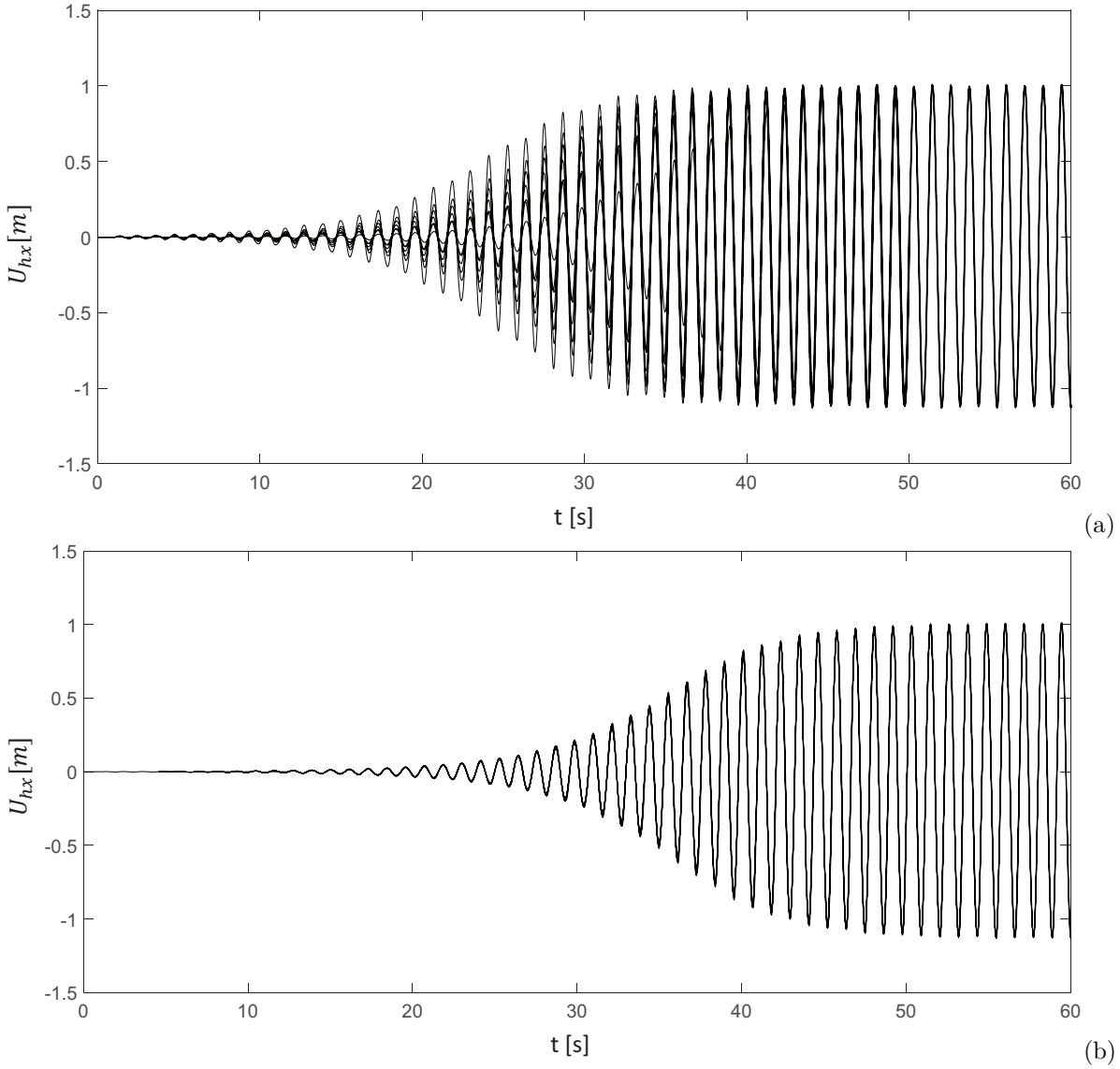

Figure 5.6: Displacement representation in various pulse at 18 m/s

Moreover, we can see in figure 5.6(b) that all the oscillating signals generated by different pulses, follow by exactly the same evolution of the amplitude with exactly the same enveloping curve, the only difference is they have delay in time and that

delay connected with the energy content of the pulse as we are going to see later. Not all of them expand with the same rate at the beginning but they attenuate with a same interaction of mechanisms and levelized finally at a same constant value in a long term, as we can see in figure 5.6(b). In order to understand the delay time and the nature of the initial expansion, we plot the same signals in the Semilog axes so we could verify the initial expansion is indeed exponential because all of the enveloping curve that we have seen represented by a clear straight lines which are parallel. In figure 5.7(a) we can see all this initial expansion are characterize exactly by a same λ which is the slope of the curve but they have the delay time which is equal to what we show to synchronize the curves in figure 5.6(b). So figure 5.7(a) shows that parallel λ and we can identify this delay time by measuring horizontally shift of all these linear relations in the semilog plot for the different combination of pulses with different energy content, when we applied that delay we can again pile up together in a semilog version as shown in figure 5.7(b).

$$U_h = A_0 e^{-\lambda(t-td)} \tag{5.1}$$

$$U_{h_{ref}} = A_{0_{ref}} e^{-\lambda(t)} \tag{5.2}$$

$$A_{0_{ref}} e^{-\lambda(t)} = A_0 e^{-\lambda(t-td)} \tag{5.3}$$

$$\frac{A_{0_{ref}}}{A_0} = \frac{e^{-\lambda(t)} e^{-\lambda(t_d)}}{e^{-\lambda(t)}} \tag{5.4}$$

$$t_d = (1/\lambda) \ln(A_{0_{ref}}/A_0) \tag{5.5}$$

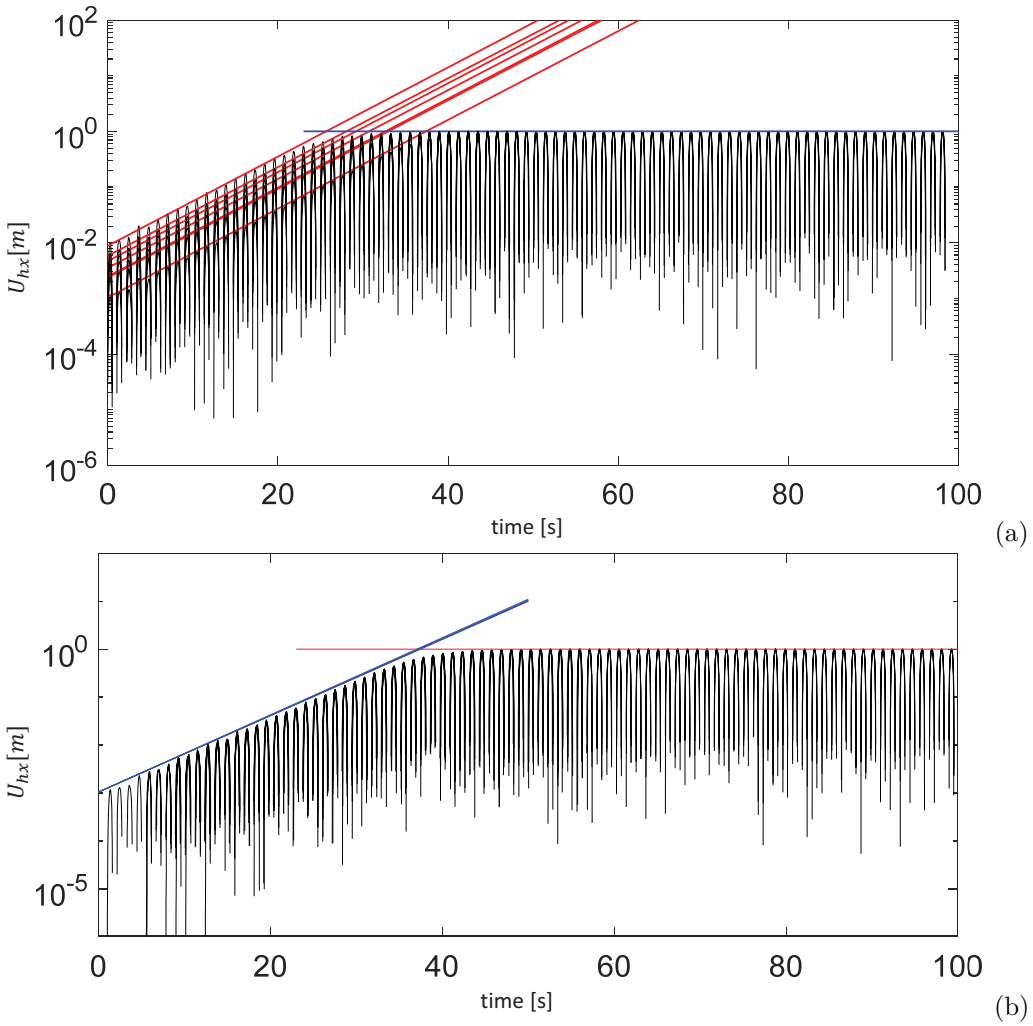

Figure 5.7: characterization of the expansion of various pulse at 18 m/s by a same λ in Semilog coordinate

The objective of the figure 5.6 is to show all the curves evolve in the same manner at the beginning with an expansion and all in the cases regardless of the energy of the pulses we observe the same attenuation when the second mechanism starts to act and finally reaching the plateau which is same for all the cases. Essentially we have two mechanisms which the first one is absorbing the energy from the free flow and

the other dissipating the energy absorbed by the system , regardless of the origin of the pulse that initiate the oscillation.

$$U_h = A_0 e^{-\lambda(t)} \tag{5.6}$$

$$\hat{U_{h_{ref}}} = A_0 e^{-\lambda(t_{ref})} \tag{5.7}$$

$$\hat{U_h} = A_0 e^{-\lambda(t_{ref} - t_d)} \tag{5.8}$$

$$\hat{U_h} = A_0 e^{-\lambda(t_{ref}} e^{\lambda(t_d)} \tag{5.9}$$

$$\hat{U_h} = \hat{U_{h_{ref}}} e^{\lambda(t_d)} \tag{5.10}$$

$$\frac{\hat{U_h}}{PulsEn} = Flexel \tag{5.11}$$

$$\hat{U_{h_{ref}}} = Flexel.PulsEn \tag{5.12}$$

$$t_{ref} = \frac{1}{-\lambda} Ln\left(\frac{\hat{U_{h_{ref}}}}{A_0}\right) \tag{5.13}$$

$$\hat{U_h} = Flexel.PulsEn \tag{5.14}$$

$$\frac{\hat{U_h}}{\hat{U_{h_{ref}}}} = e(\lambda t_d) \tag{5.15}$$

$$\frac{Flexel.PulsEn}{Flexel.PulsEn_{ref}} = e^{(}\lambda t_d) \tag{5.16}$$

$$Ln\left(\frac{Flexel.PulsEn}{Flexel.PulsEn_{ref}}\right) = \lambda(t_d) \tag{5.17}$$

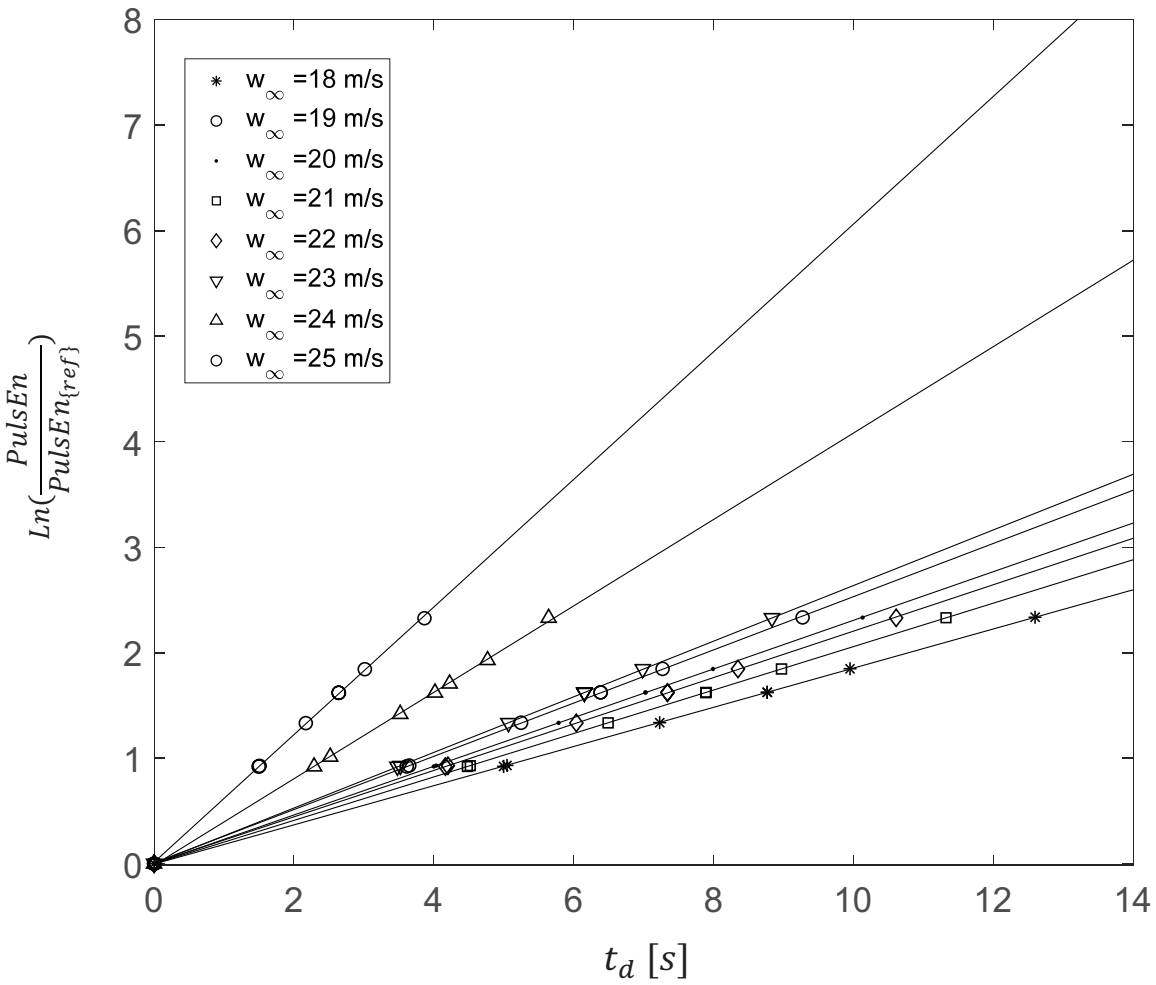

Figure 5.8: Initial energy delivered by the pulse at unstable oscillatory region

We are going to have a double confirmation of the energy principal. We have verified that there is an exponential expansion at the beginning and all the various pulse configuration will coincident with time delay according to the energy of the pulse. When we collapse all of them together they will exactly follow one after the other and on the Semilog plot they are parallel lines that they shifted in the time and they

collapsed in straight lines that proof the exponential expansion with the determined λ which is essentially the same thing that we have observed in stable oscillation region but this time instead of being damping it has amplification, and the λ depends only on velocity (figure 5.9).

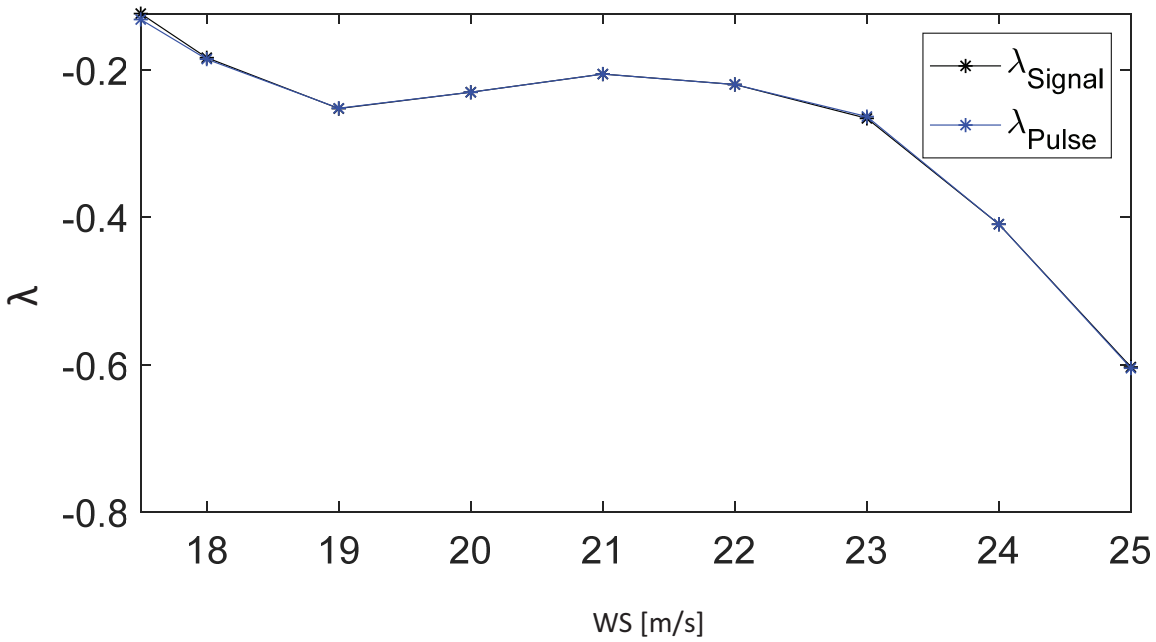

Figure 5.9: Double confirmation of the energy principal in unstable oscillatory region

Moreover, different time span gust also aligned in the same straight line so we can conclude that, the certain delay connected to the energy of the pulse. That means there is another connection with energy principle which is related with the starting point of that exponential expansion and that starting point related with amount of energy delivered by the pulse onto the system, so after the pulse the system continues

extracting energy from the flow with the same λ. So that seems to indicate that we have this energy absorption from the flow controlled by the same λ. Regardless of the kick that start the oscillatory expansion, another interesting thing is that when we plot the delay time , how much longer it takes to reach the same level for smaller pulses that start later to reach to the same level of elastic energy. Figure 5.8 indicates that the initial energy delivers by the pulse is equivalent to the amount of the energy that should have been extracted by the system in that exponential expansion from the flow in order to reach to that same level, so that slop in the alignment of the fiure 5.8 has to be related with the λ of the expansion of the curve later.

The amount of the energy that is delivered by the pulse, is starting the expansion at the later point on the same curve and when you project backward , what you have is pulses that have less energy need to accumulate that same amount of energy by extracting that from the flow with the same exponential law and that is why when we plot the time that is require for the system with lower energy pulses to reach to that same level that was delivered by the higher energy pulse that time is also response to the same law,evolves exponentially with time but we have to project backwards.

5.3.1 Departure Time and Destabilization Time

In figure 5.10 and figure 5.11 and, we showed different wind speeds with corresponding value of displacement and departure time.

As it is shown in figure 5.10, we can find for all wind velocities it has a same functional relation which can be related to the physical mechanism. From this relation we can get that these two mechanisms are proportional so we know the second mechanism starts to act at a certain proportion which the amount of elastic energy that starts the second mechanism to act vs the amount of energy at which the second mechanism exactly compensates the first one is the same.

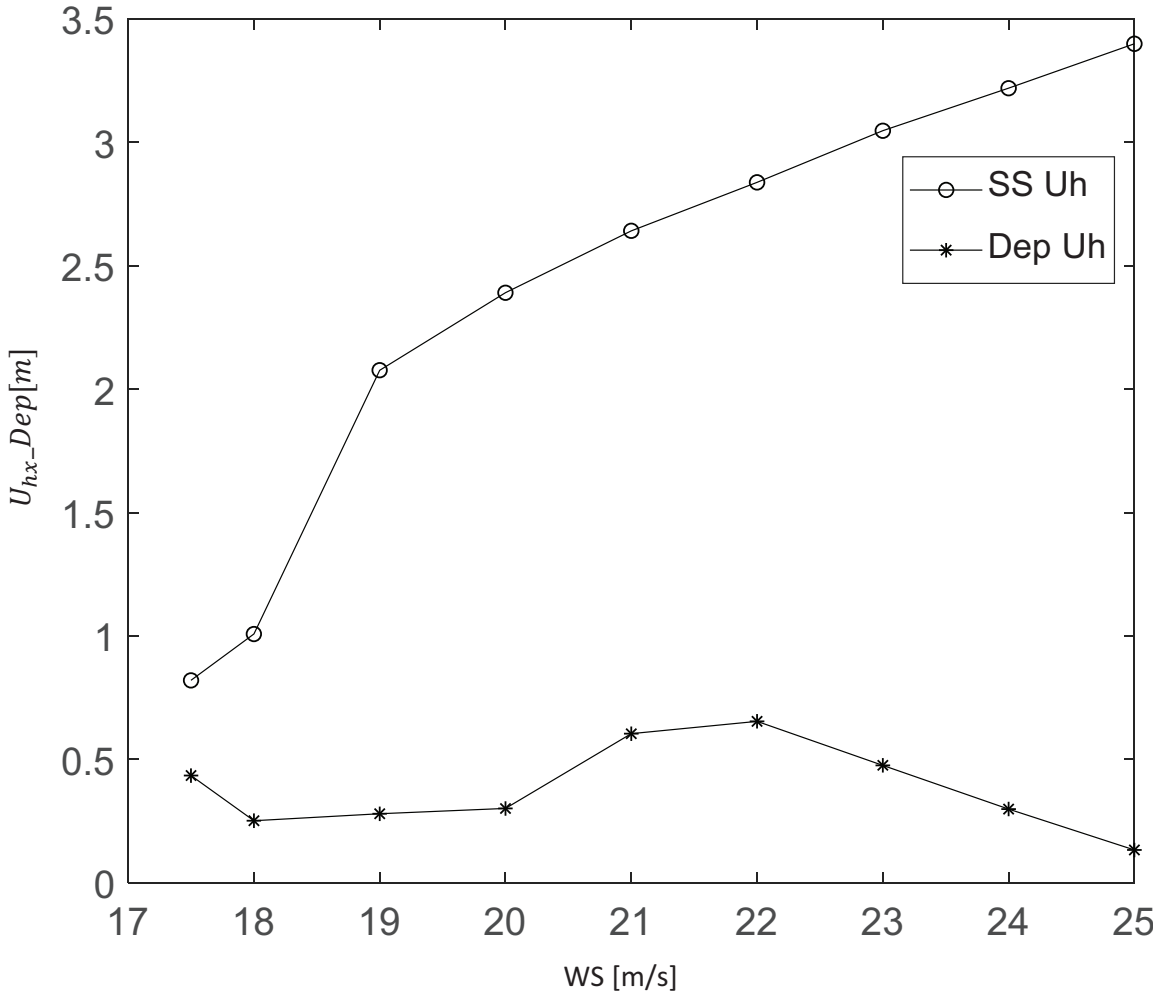

Figure 5.10: Unstable oscillatory region wind speeds with corresponding value of displacement

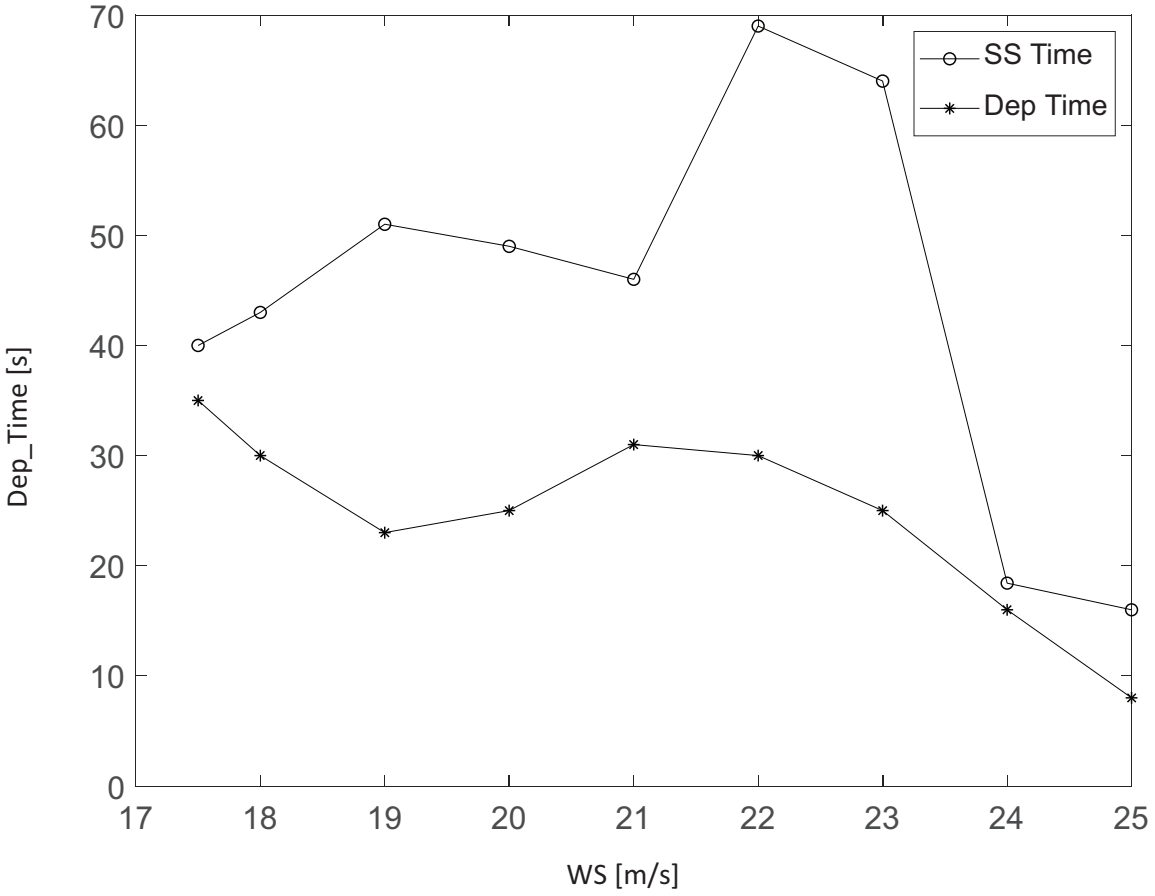

Figure 5.11: Unstable oscillatory region wind speeds with corresponding value of time

5.3.2 Frequency Content on Unstable Oscillatory Regime

As we tried in section 5.2,we are going to analyze the energy content in amplitude and we noted the same quantitative behavior which is also connected with the values of the λ that we showed in the figure 5.9 .

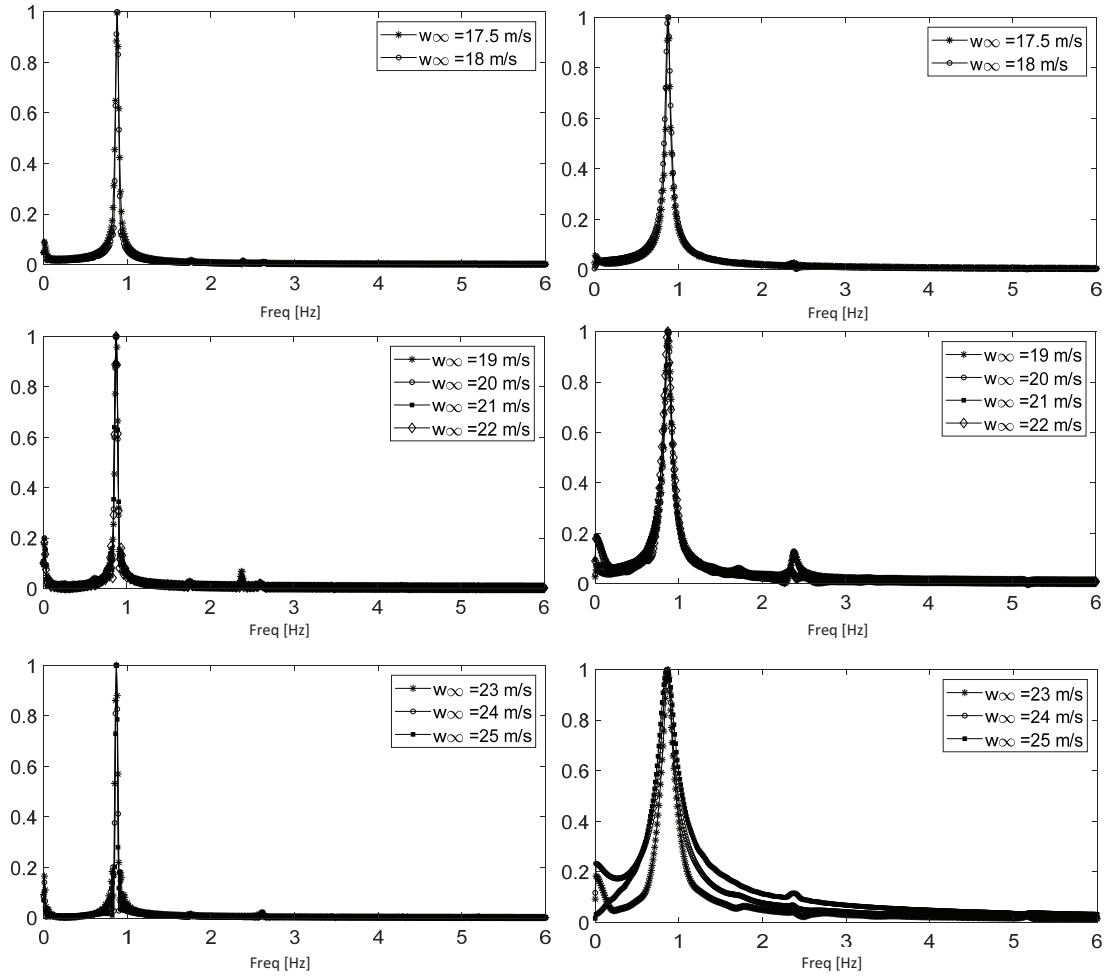

Figure 5.12: Three Groups Spectra for unstable oscillatory region, Left plots [0 49]sec, right plots [0 DT]sec

If the pulse is fast enough (i,e, if faster than 0.25 seconds, all its kinetic energy goes into elasticity, so each value of PulseEn corresponds to a certain value of U_{hEnv}. Hence, each PulseEner translates into an amount of initial elastic energy, i,e, a $U_{h_{Env_0}}$, that intersects the $U_{h_{Env}}$ curve at a certain time ($t_{PulsEnE_f}$), which corresponds to the lapse that would have taken to the system to acquire that energy from the flow

that means that, there is going to be a time advance of $t_{PulsEnE_f}$ associated with each PulseEn. In the other words, what the Pulse does is depositing an initial amount of energy into the system which,otherwise, the system would have acquired by the same exponential expansion law controlled by the same λ.

5.4 Transient Zone

Figure 4.3(c) shows the evolution for the threshold itself, where the amplitude after the initial kick from the gust remains constant. Figure 4.3(d) illustrates the characteristic frequency content of the evolution at the threshold. This is typical of threshold conditions that we have observed in our experiments, which show the fundamental frequency, plus harmonic and quasi-periodic components. This frequency richness exhibited at the threshold encompasses several forms of oscillatory behavior spread over the timespan of the simulation. For more detail see paper Jalal et al. [49]

From Jalal et al. [49], it could be seen that the system starts oscillating at a frequency mostly dominated by the fundamental component of 0.88 Hz, and gradually evolves into a more complex behavior where two quasi-periodic components of 1.26 Hz and 2.4 Hz and a sixth harmonic of 5.14 Hz become equally important. The evolution continues, where the fundamental progressively gives way until it practically disappears, and the other two components become totally dominant.

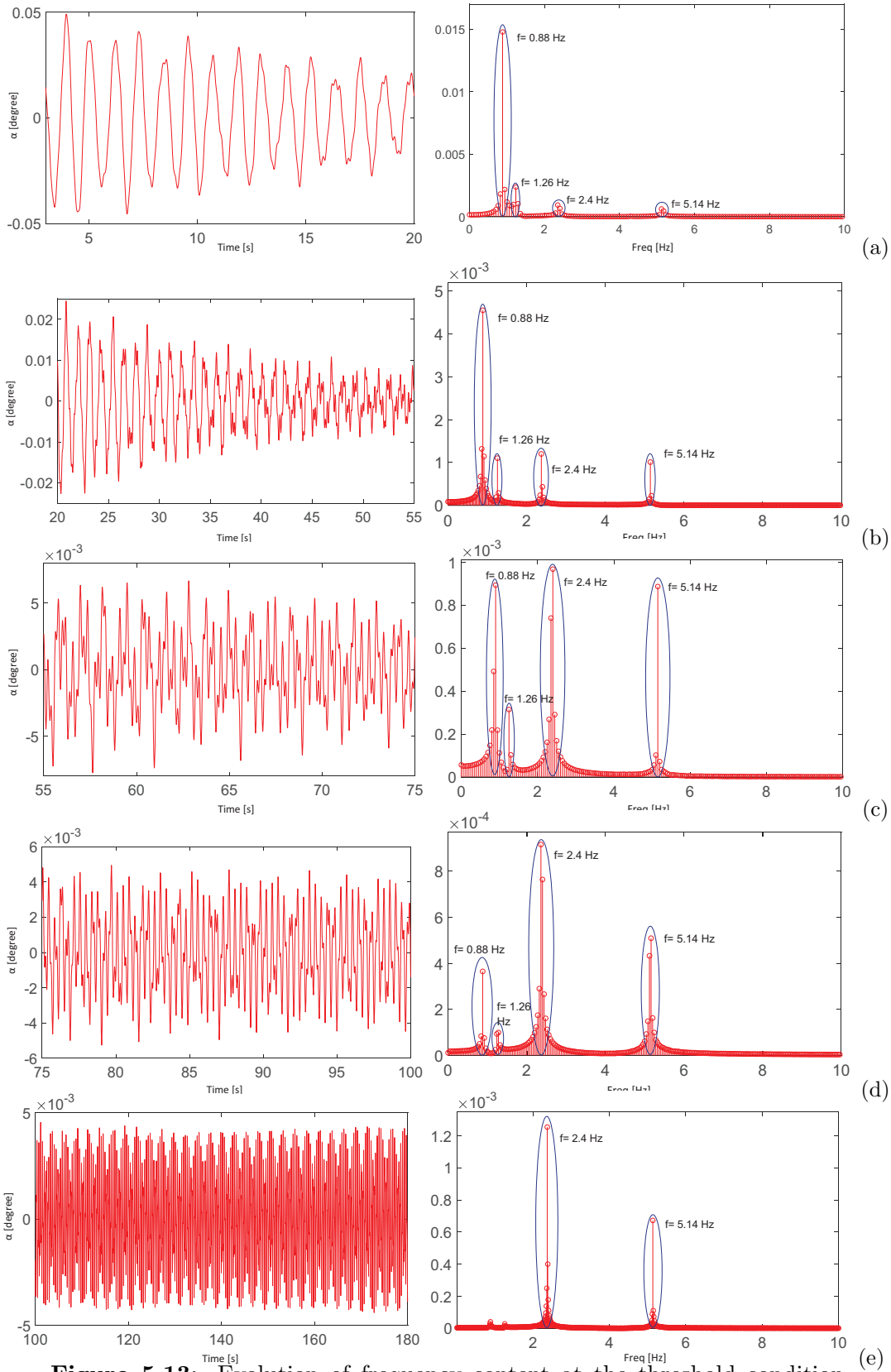

Figure 5.13: Evolution of frequency content at the threshold condition through different time segments.

Chapter 6

Conclusions

In this thesis work we have studied the pure aero-elasto-inertial dynamics of stall-controlled wind turbine rotors as oscillatory systems. We have shown the results from an extensive series of experiments analyzing the dynamic response of the rotor to wind speed fluctuations associated to the turbulent characteristics of the atmospheric boundary layer, obtaining a reduced-order characterization of the rotor's dynamics as an oscillatory system based on energy-transfer principles.

Besides on its intrinsic scientific value, this aspect of the work presented here is of fundamental interest for researchers and engineers working on developing optimized control strategies for wind turbines. It allows for the critical elements of the rotor's dynamic behavior to be described as a reduced-order model that can be solved in

real-time, an essential requirement for determining predictive control actions. These are critical in terms of the mitigation of peak structural loads, the stability of turbine operational parameters like torque and power output, and reducing the accumulation of fatigue efforts.

As and outlook for further work, we envision a series of experiments exploring the dynamics of the rotor when subjected to wind speed pulses of longer duration. Differently from what it happens in the short pulses associate with the turbulent content of the wind flow, in these cases, the kinetic energy content of the pulse is delivered during a period of time which is comparable or longer than the period of the first peak of the displacement oscillation. The consequence of which is that the aerodynamic damping has time to act during the duration of the pulse itself, dissipating a non-negligible part of the energy of the gust pulse before it gets accumulated as elastic energy in the blade deflection. In this range of longer pulse time scales, the energy-transfer principle is still expected to operate, but with the evolution of the blade-deflection peaks evolving in a different manner.

References

[1] IEC, Wind Turbine Generator Systems – Part 13: Measurement of mechanical loads, Report IEC/TS 61400–13, International Electrotechnical Commission (IEC), 2001.

[2] H. J. Sutherland, Analysis of the structural and inflow data from the list turbine, J. Sol. Energy Eng. 124 (2002) 432–445.

[3] A. M. M. Ismaiel, S. Yoshida, Study of turbulence intensity effect on the fatigue lifetime of wind turbines, Evergreen 5 (2018) 25–32.

[4] T. Senjyu, R. Sakamoto, N. Urasaki, T. Funabashi, H. Fujita, H. Sekine, Output power leveling of wind turbine generator for all operating regions by pitch angle control, IEEE Transactions on Energy Conversion 21 (2006) 467–475.

[5] G. Lalor, A. Mullane, M. O'Malley, Frequency control and wind turbine technologies, IEEE Transactions on Power Systems 20 (2005) 1905–1913.

[6] N. Deshpande, Computational analysis of the aeroelastic dynamics of a wind turbine blade with variable-speed stall control, Master's thesis, Michigan Technological University, 2015.

[7] J. Slootweg, S. De Haan, H. Polinder, W. Kling, General model for representing variable speed wind turbines in power system dynamics simulations, IEEE Transactions on Power Systems 18 (2003) 144–151.

[8] N. Fichaux, J. Beurskens, P. H. Jensen, J. Wilkes, S. Frandsen, J. Sorensen, P. Eecen, C. Malamatenios, J. Gomez, J. Hemmelmann, et al., Upwind: Design limits and solutions for very large wind turbines, Sixth Framework Programme (2011).

[9] N. Hodge, G. C. Stocks, Wind energy companies: A snapshot of the global wind industry, 2008. URL: `www.greenchipstocks.com`.

[10] J. G. Stuart, A. D. Wright, C. P. Butterfield, Wind turbine control systems: dynamic model development using system identification and the FAST structural dynamics code, Technical Report NREL/TP–440-22081, National Renewable Energy Laboratory, Golden, CO (United States), 1996.

[11] T. K. Barlas, G. A. M. Van Kuik, State of the art and prospectives of smart rotor control for wind turbines, in: Journal of Physics: Conference Series, volume 75, IOP Publishing, 2007, p. 012080.

[12] J. W. V. Wingerden, A. W. Hulskamp, T. Barlas, B. Marrant, G. A. M. V. Kuik, D. P. Molenaar, M. Verhaegen, On the proof of concept of a 'smart'wind turbine rotor blade for load alleviation, Wind Energy 11 (2008) 265–280.

[13] F. D. Bianchi, H. De Battista, R. J. Mantz, Wind turbine control systems: principles, modelling and gain scheduling design, Springer Science & Business Media, 2006.

[14] E. Muljadi, K. Pierce, P. Migliore, Control strategy for variable-speed, stall-regulated wind turbines, in: Proceedings of the 1998 American Control Conference. ACC (IEEE Cat. No.98CH36207), volume 3, 1998, pp. 1710–1714.

[15] E. Muljadi, C. P. Butterfield, Pitch-controlled variable-speed wind turbine generation, IEEE Transactions on Industry Applications 37 (2001) 240–246.

[16] J. I. Herrera, T. W. Reddoch, J. S. Lawler, Harmonics generated by two variable speed wind generating systems, IEEE Transactions on Energy Conversion 3 (1988) 267–273.

[17] M. Steinbuch, Optimal multivariable control of a wind turbine with variable speed, Wind Engineering 11 (1987) 153–163.

[18] H. Polinder, D. Bang, R. P. J. O. M. van Rooij, A. S. McDonald, M. A. Mueller, 10 mw wind turbine direct-drive generator design with pitch or active speed stall control, in: 2007 IEEE International Electric Machines & Drives Conference, volume 2, 2007, pp. 1390–1395.

[19] C. L. Bottasso, A. Croce, F. Gualdoni, P. Montinari, Load mitigation for wind turbines by a passive aeroelastic device, Journal of Wind Engineering and Industrial Aerodynamics 148 (2016) 57–69.

[20] Z. Salameh, Operation of the variable speed constant frequency double output induction generator (vscf-doig) in a constant optimum power coefficient mode, Wind Engineering 9 (1985) 67–75.

[21] K. H. Hohenemser, A. H. P. Swift, On the design of horizontal axis two-bladed hinged wind turbines, Journal of Solar Energy Engineering 106 (1984) 171–176.

[22] E. J. N. Menezes, A. M. Araújo, N. S. B. da Silva, A review on wind turbine control and its associated methods, Journal of Cleaner Production 174 (2018) 945–953.

[23] Z. Lubosny, J. W. Bialek, Supervisory control of a wind farm, IEEE transactions on power systems 22 (2007) 985–994.

[24] J. F. Manwell, J. G. McGowan, A. L. Rogers, Wind energy explained: Theory, design and application, Wiley, Chichester, UK, 2009.

[25] T. Burton, D. Sharpe, N. Jenkins, E. Bossanyi, Wind Energy Handbook, Wiley, Chichester, UK, 2001.

[26] D. Bang, H. Polinder, J. Ferreira, R. Van Rooij, A new active speed stall control

compared to pitch control for a direct-drive wind turbine, in: EWEC 2007 Conference proceedings, 2007, EWEA European Wind Energy Association, 2007.

[27] E. Muljadi, K. Pierce, P. Migliore, Soft-stall control for variable-speed stall-regulated wind turbines, Journal of Wind Engineering and Industrial Aerodynamics 85 (2000) 277–291.

[28] A. D. Hansen, C. Jauch, P. E. Sørensen, F. Iov, F. Blaabjerg, Dynamic wind turbine models in power system simulation tool DIgSILENT, 2004.

[29] A. Miller, E. Muljadi, D. S. Zinger, A variable speed wind turbine power control, IEEE Transactions on Energy Conversion 12 (1997) 181–186.

[30] R. Thresher, S. Schreck, M. Robinson, P. Veers, Wind energy status and future wind engineering challenges, Technical Report NREL/CP-500-43799, National Renewable Energy Lab, 2008.

[31] O. G. Jaimes, Design concepts for offshore wind turbines: a technical and economical study on the trade-off between stall and pitch controlled systems, Ph.D. thesis, MSc Thesis, Delft University of Technology, 2010.

[32] J. Jonkman, S. Butterfield, W. Musial, G. Scott, Definition of a 5-MW reference wind turbine for offshore system development, Technical Report NREL/TP-500-38060, National Renewable Energy Laboratory, 2009.

[33] F. L. Ponta, A. D. Otero, L. I. Lago, A. Rajan, Effects of rotor deformation in wind-turbine performance: The dynamic rotor deformation blade element momentum model (drd–bem), Renewable Energy 92 (2016) 157–170.

[34] F. L. Ponta, P. M. Jacovkis, A vortex model for Darrieus turbine using finite element techniques, Renewable Energy 24 (2001) 1–18.

[35] H. Glauert, The analysis of experimental results in the windmill brake and vortex ring states of an airscrew, Technical Report Reports and Memoranda Volume 1026, Great Britain Aeronautical Research Committee, 1926.

[36] H. Glauert, Airplane propellers, in: Aerodynamic theory, Springer, 1935, pp. 169–360.

[37] C. Crawford, Re-examining the precepts of the blade element momentum theory for coning rotors, Wind Energy 9 (2006) 457–478.

[38] R. Lanzafame, M. Messina, Fluid dynamics wind turbine design: Critical analysis, optimization and application of {BEM} theory, Renewable Energy 32 (2007) 2291 – 2305.

[39] J. G. Leishman, T. S. Beddoes, A generalised model for airfoil unsteady aerodynamic behaviour and dynamic stall using the indicial method, in: 42nd. Annual Forum of the American Helicopter Society, Washington D. C, 1986, pp. 243–266.

[40] A. D. Otero, F. L. Ponta, Structural analysis of wind-turbine blades by a generalized Timoshenko beam model, Journal of Solar Energy Engineering 132 (2010) 011015.

[41] D. A. Griffin, Blade System Design Studies Volume I: Composite Technologies for Large Wind Turbine Blades, Report SAND2002-1879, Sandia National Laboratories, 2002.

[42] W. Yu, D. H. Hodges, V. Volovoi, C. E. S. Cesnik, On Timoshenko-like modeling of initially curved and twisted composite beams, Int. J. Sol. and Struct. 39 (2002) 5101–5121.

[43] D. H. Hodges, Nonlinear Composite Beam Theory, AIAA, Reston, Virginia, 2006.

[44] P. Jamieson, Innovation in wind turbine design, Wiley, 2011.

[45] C. Crawford, J. Platts, Updating and optimization of a coning rotor concept, Journal of Solar Energy Engineering 130 (2008) 031002.

[46] M. Menon, F. Ponta, Dynamic aeroelastic behavior of wind turbine rotors in rapid pitch-control actions, Renewable Energy 107 (2017) 327–339.

[47] A. D. Otero, F. L. Ponta, On the sources of cyclic loads in horizontal-axis wind turbines: The role of blade-section misalignment, Renewable Energy 117 (2018) 275–286.

[48] W. Xudong, W. Z. Shen, W. J. Zhu, J. Sorensen, C. Jin, Shape optimization of wind turbine blades, Wind Energy 12 (2009) 781–803.

[49] S. Jalal, F. Ponta, A. Baruah, Aeroelastic response of variable-speed stall-controlled wind turbine rotors, in: ASME 2019 13th International Conference on Energy Sustainability, American Society of Mechanical Engineers, 2019, pp. ES2019–3803.

Appendix A

Blade-Deflection Plots for the Stable Oscillatory Regime of Wind Speeds

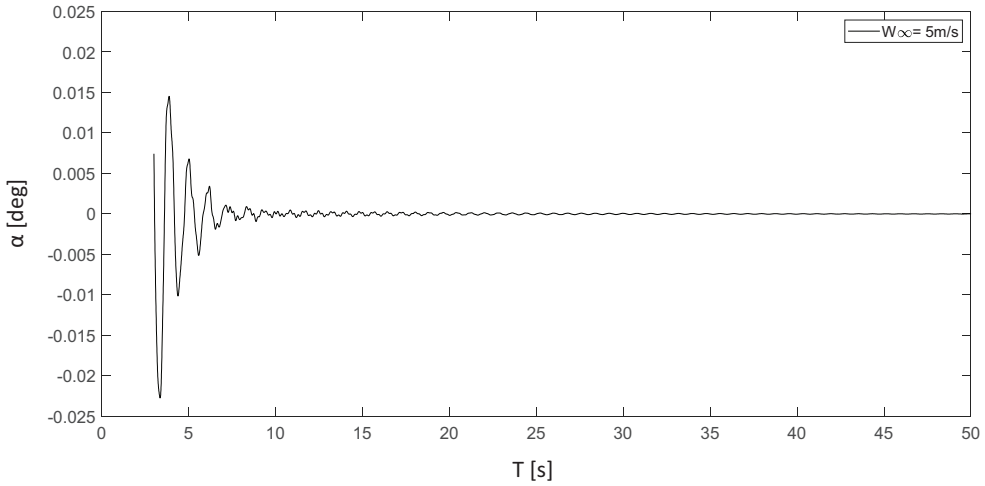

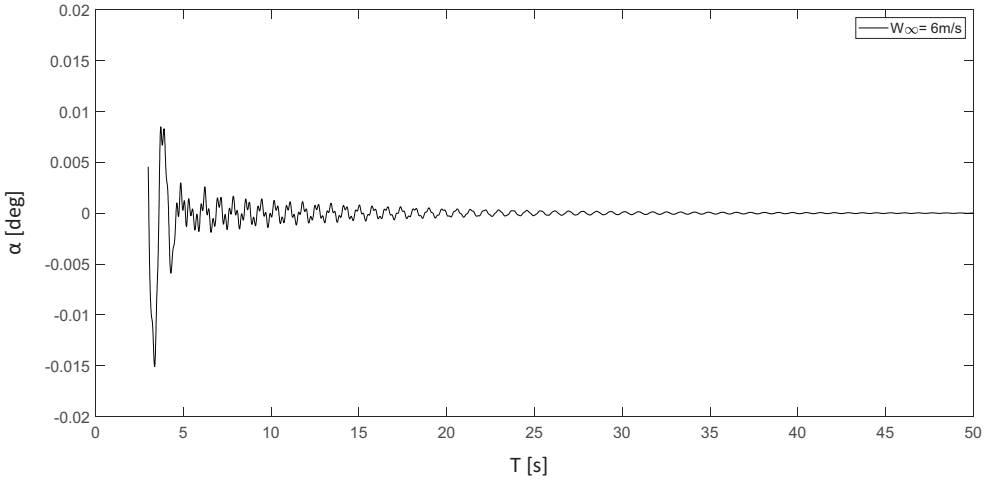

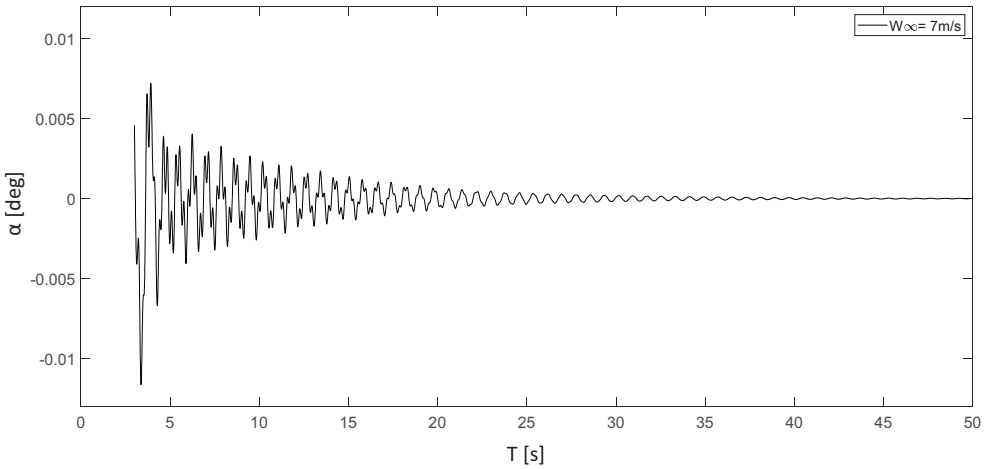

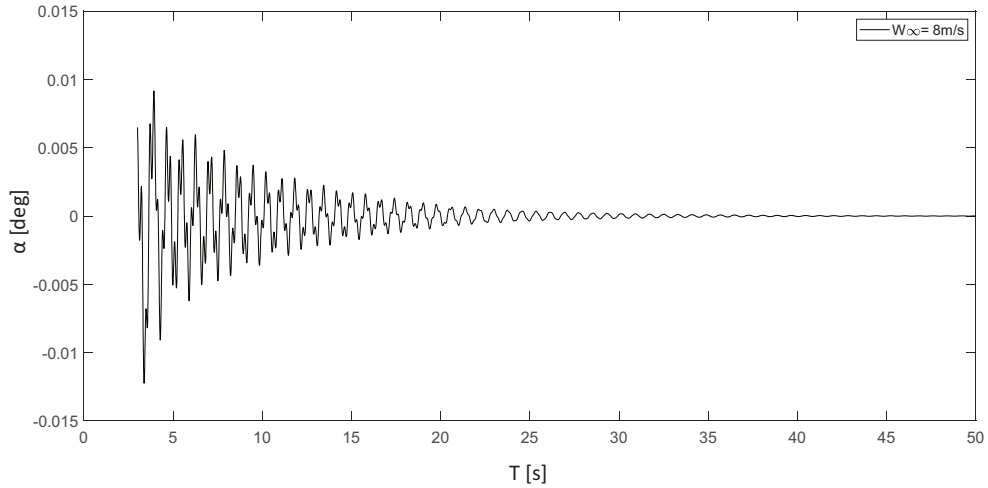

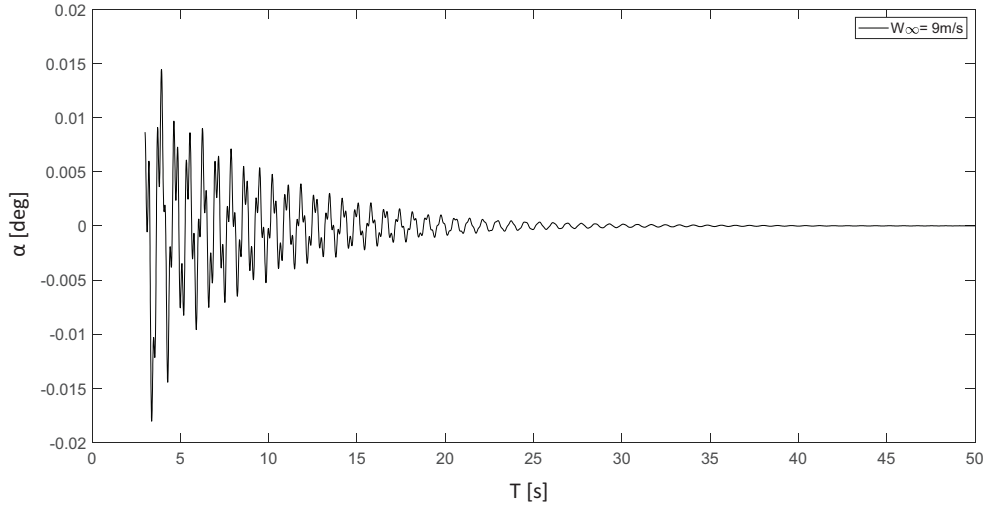

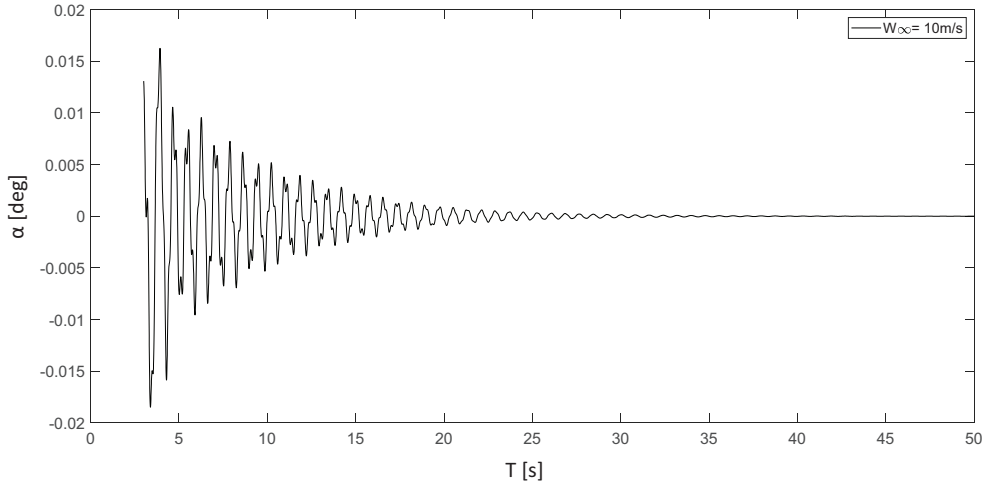

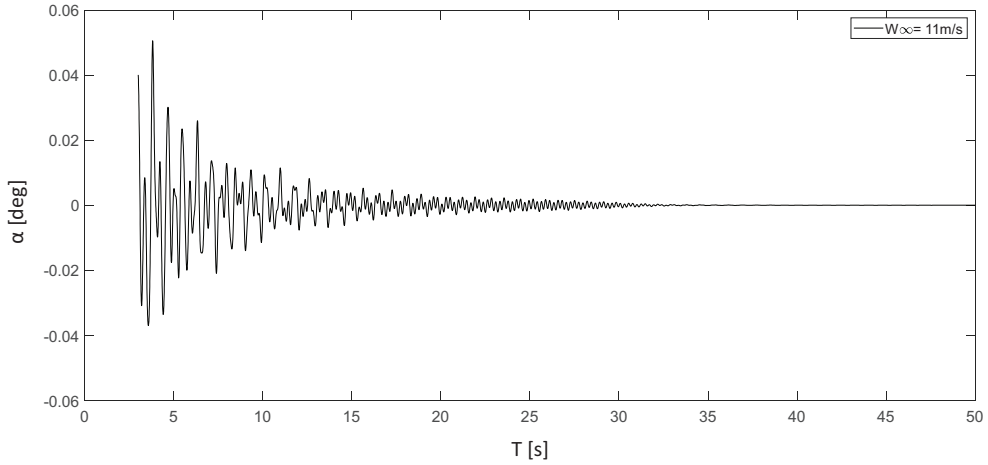

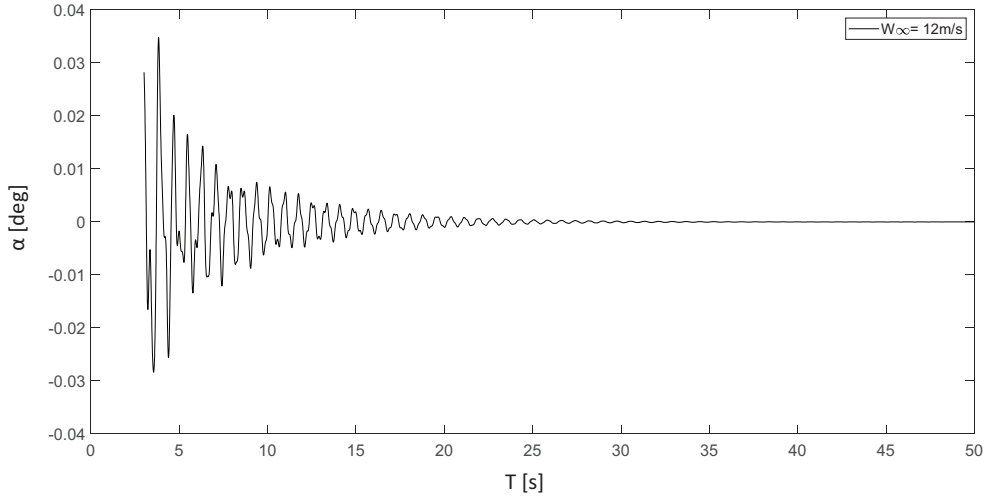

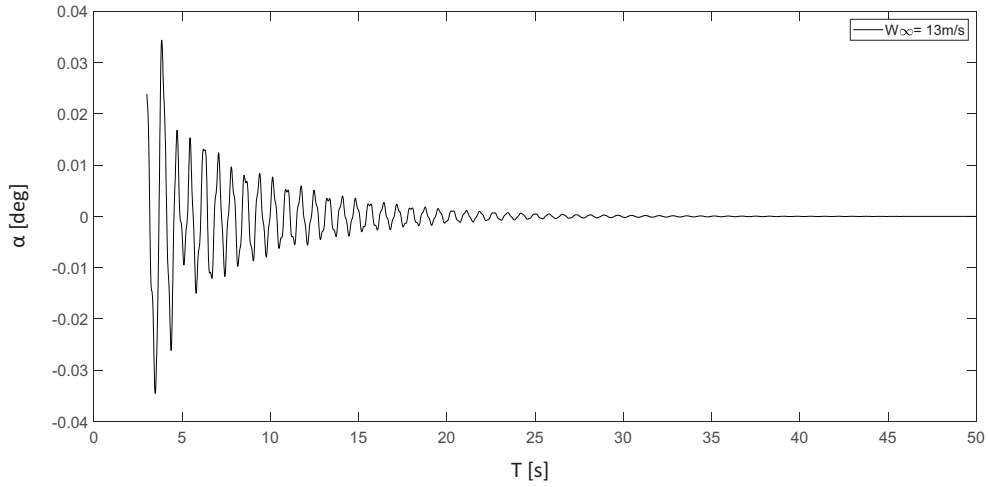

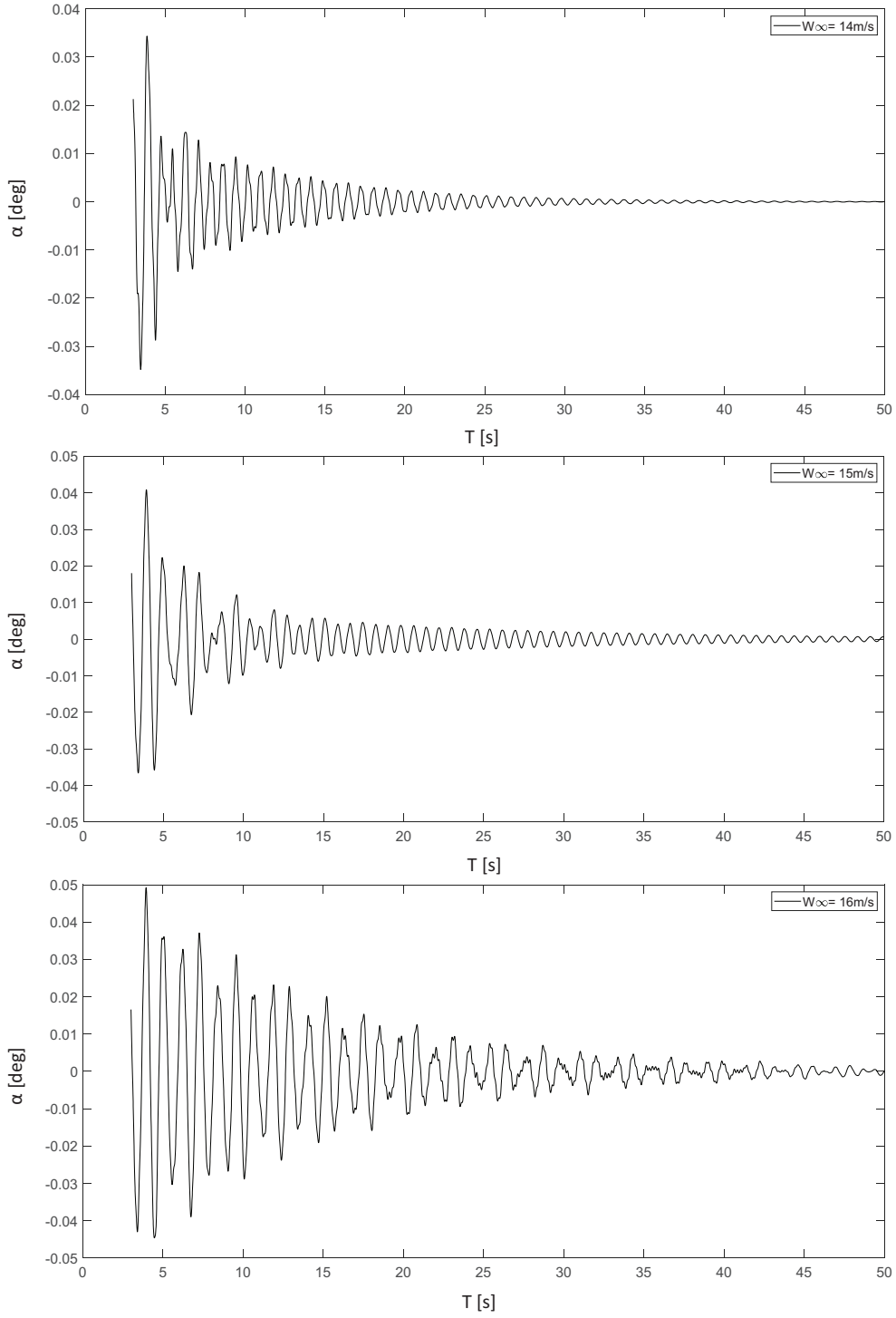

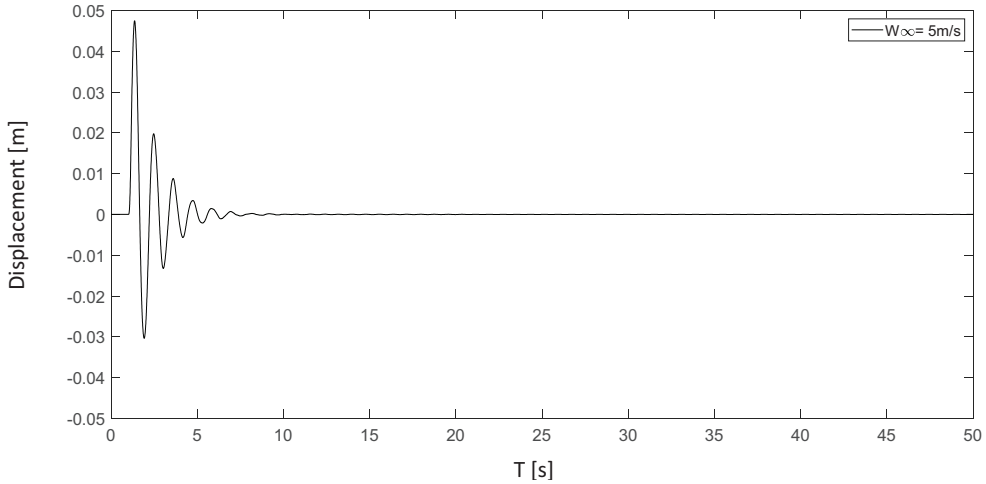

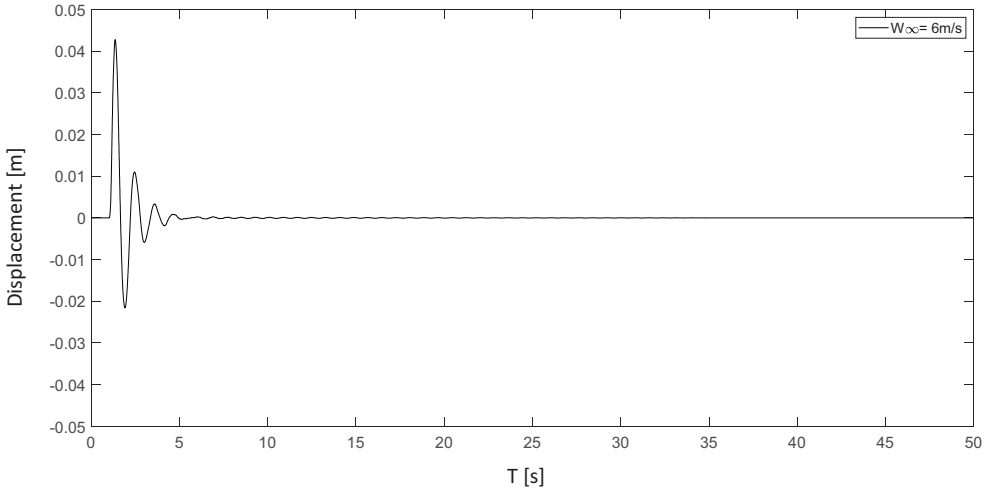

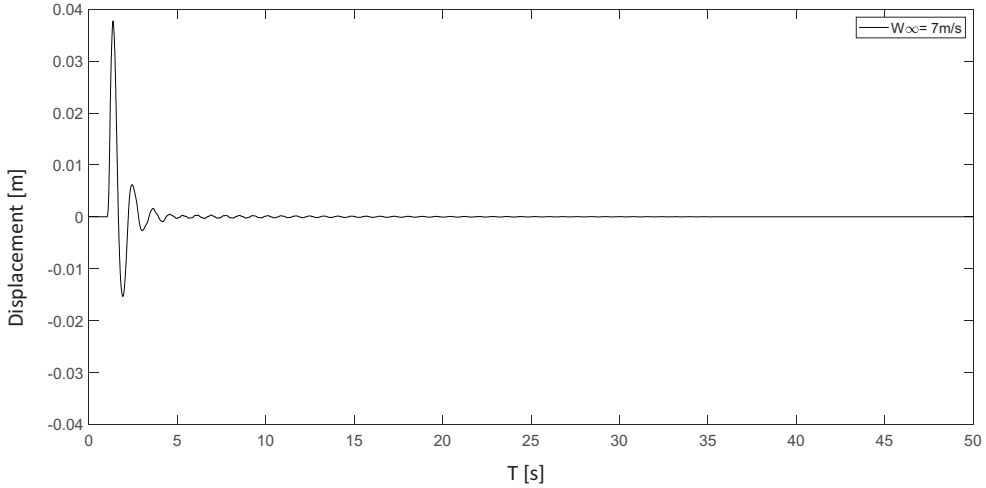

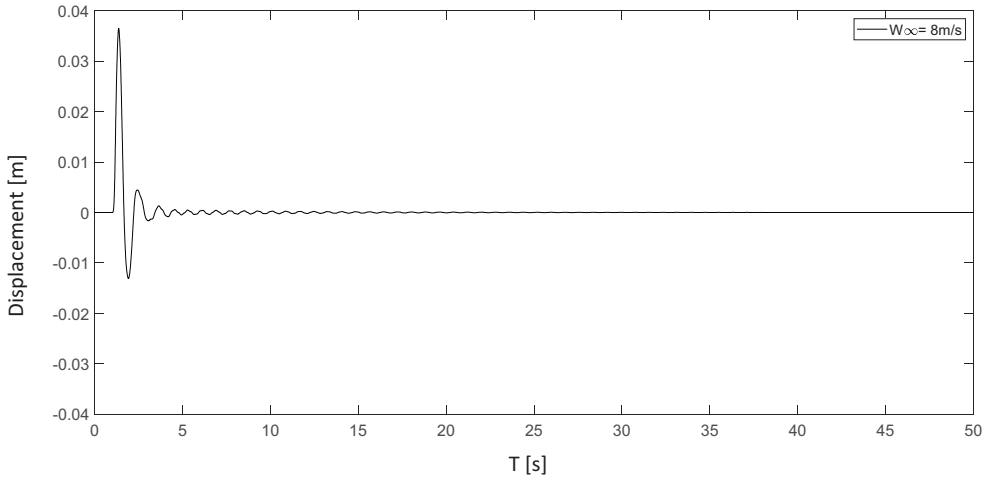

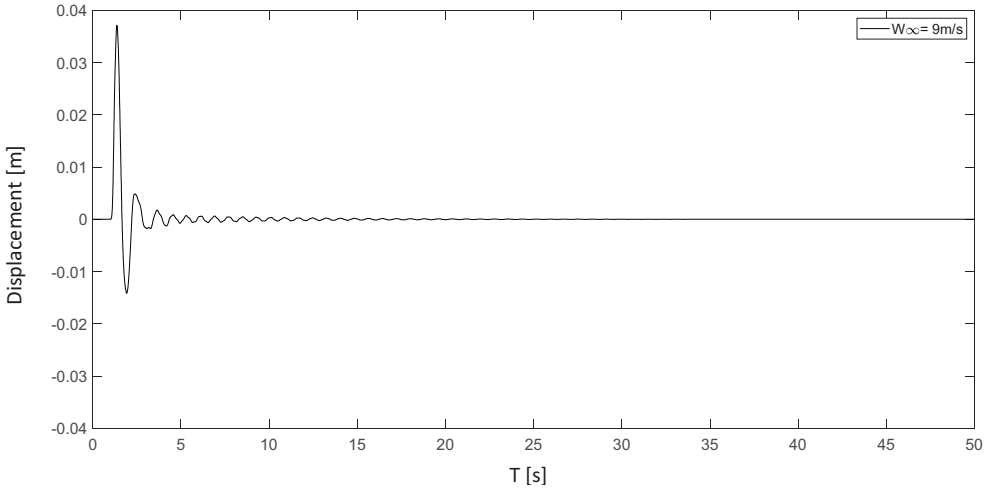

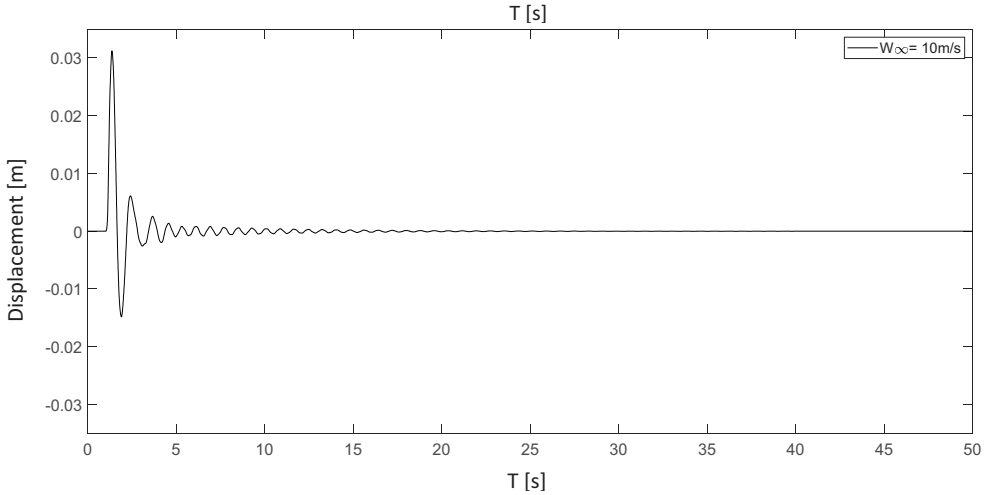

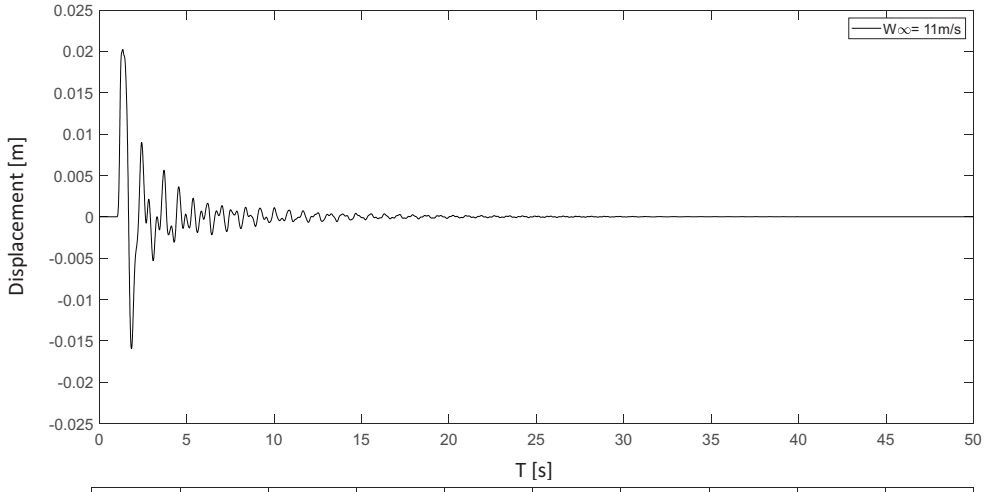

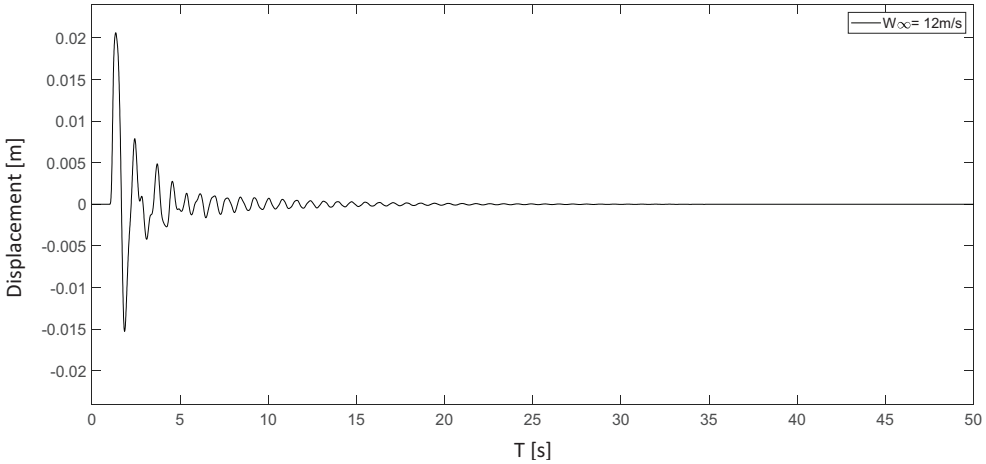

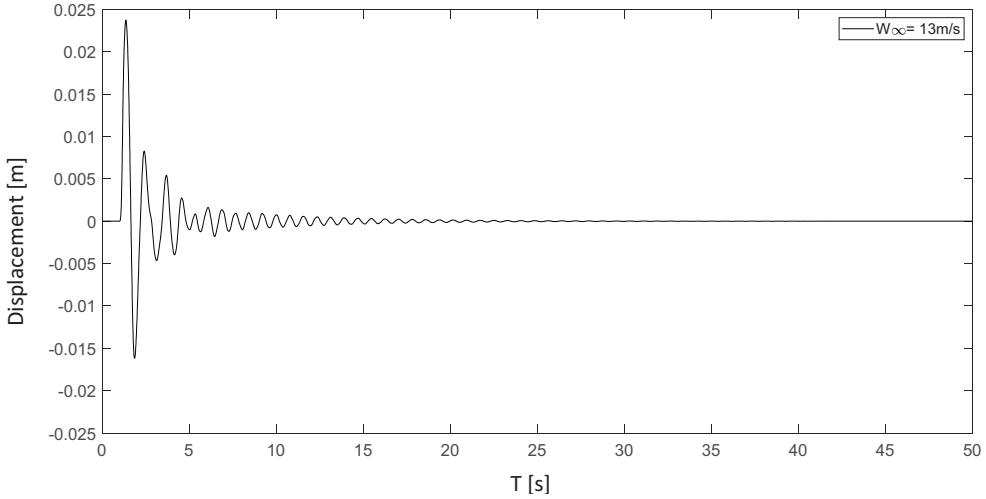

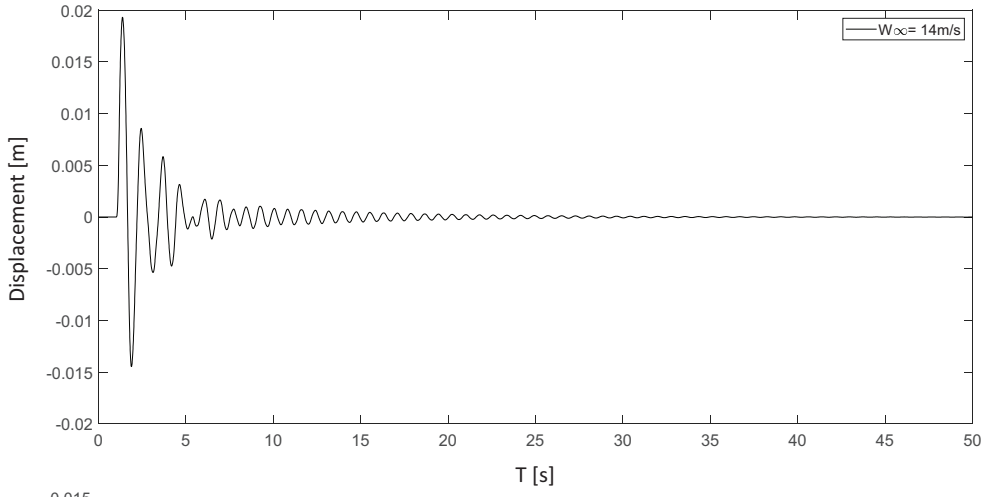

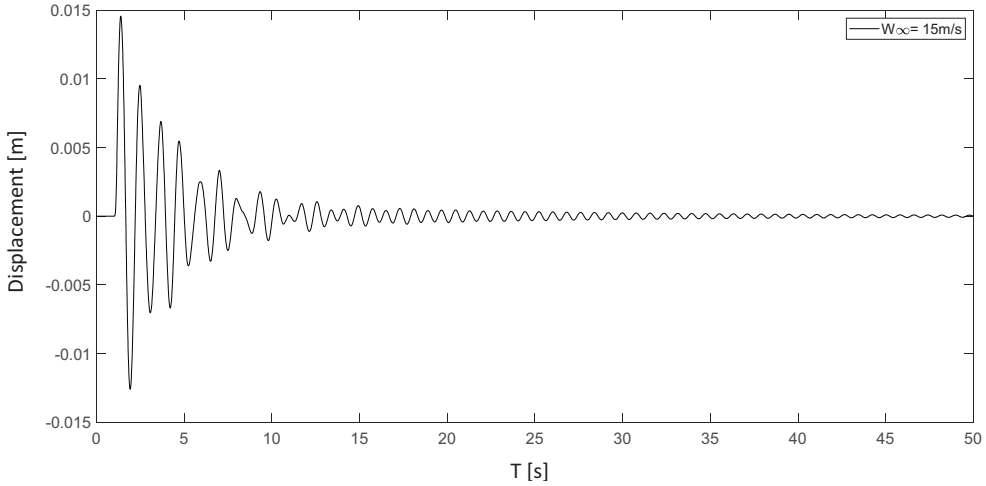

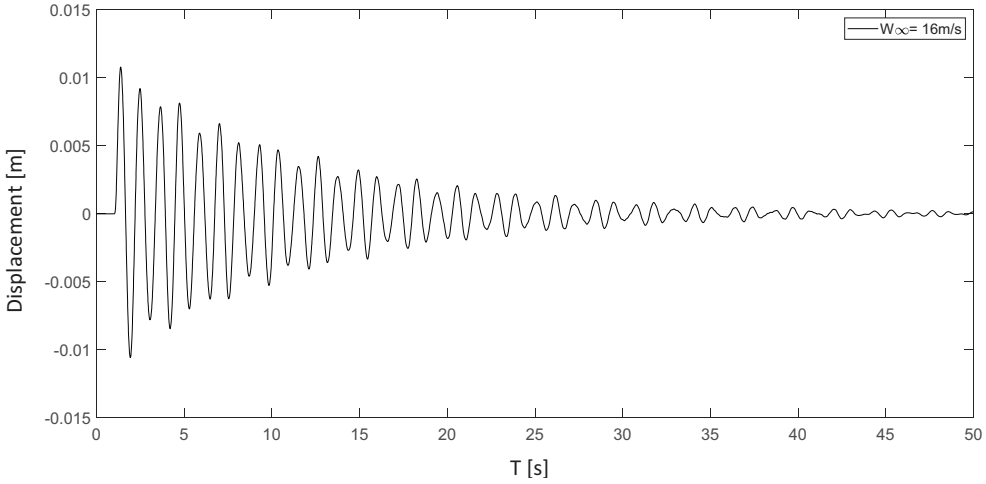

Appendix B

Blade-Deflection Plots for the Unstable Oscillatory Regime of Wind Speeds